


Robust *ab initio* predictions for dimensionless ratios of $E2$ and radius observables.

I. Electric quadrupole moments and deformation

Mark A. Caprio 

Department of Physics and Astronomy, University of Notre Dame, Notre Dame, Indiana 46556-5670, USA

Pieter Maris 

Department of Physics and Astronomy, Iowa State University, Ames, Iowa 50011-3160, USA

(Dated: September 9, 2024)

Converged results for $E2$ observables are notoriously challenging to obtain in *ab initio* no-core configuration interaction (NCCI) approaches. Matrix elements of the $E2$ operator are sensitive to the large-distance tails of the nuclear wave function, which converge slowly in an oscillator basis expansion. Similar convergence challenges beset *ab initio* prediction of the nuclear charge radius. However, we exploit systematic correlations between the calculated $E2$ and radius observables to yield meaningful predictions for relations among these observables. In particular, we examine *ab initio* predictions for dimensionless ratios of the form Q/r^2 , for nuclei throughout the p shell. Meaningful predictions for electric quadrupole moments may then be made by calibrating to the ground-state charge radius, if experimentally known, or *vice versa*. Moreover, these dimensionless ratios provide *ab initio* insight into the nuclear quadrupole deformation.

I. INTRODUCTION

Converged *ab initio* predictions for nuclear electric quadrupole ($E2$) observables, including transition strengths and moments, are challenging to obtain [1–6]. *Ab initio* no-core configuration interaction (NCCI), or no-core shell-model (NCSM), calculations [7] rely upon a Slater determinant expansion of the wave function (conventionally in an oscillator basis) and must, in practice, be carried out in a finite, truncated basis. The results are only approximations to the true values which would be obtained by solving the full, untruncated many-body problem. Long-range observables, *i.e.*, those which are sensitive to the large-distance tails of the nuclear wave function, such as $E2$ matrix elements, are slowly convergent in NCCI calculations, as these tails are described only with difficulty in an oscillator-basis expansion. Including a sufficiently large basis to obtain meaningful predictions often becomes computationally prohibitive.

Nonetheless, one may exploit systematic correlations among calculated observables to yield meaningful predictions for relations among these observables, even where the observables individually are not adequately converged. The convergence patterns of calculated $E2$ matrix elements may be strongly correlated [8], especially for $E2$ matrix elements among states sharing similar structure, *e.g.*, members of low-lying rotational bands [8–11] or mirror states [12, 13]. Thus, most naturally, if a single $E2$ observable is well-known from experiment, a meaningful prediction may then be made for the other, correlated matrix elements [8]. In particular, the ground-state quadrupole moment is precisely measured in many nuclei [14], as summarized for p -shell nuclei in Fig. 1. In these cases, the known ground-state quadrupole moment provides a calibration reference, permitting $E2$ transition strengths to be estimated based on robust *ab initio* NCCI predictions for $B(E2)/(eQ)^2$. This approach

is illustrated for various light p -shell nuclei ($A \leq 9$) in Ref. [15]. Predictions for $B(E2)/(eQ)^2$ are also considered for several C isotopes (and ^{10}Be) in Ref. [16].

However, calibration to the ground-state quadrupole moment is subject to the limitation that only states with angular momentum $J \geq 1$ admit a nonvanishing quadrupole moment. Thus, notably, calibration to the ground-state quadrupole moment is not possible for even-

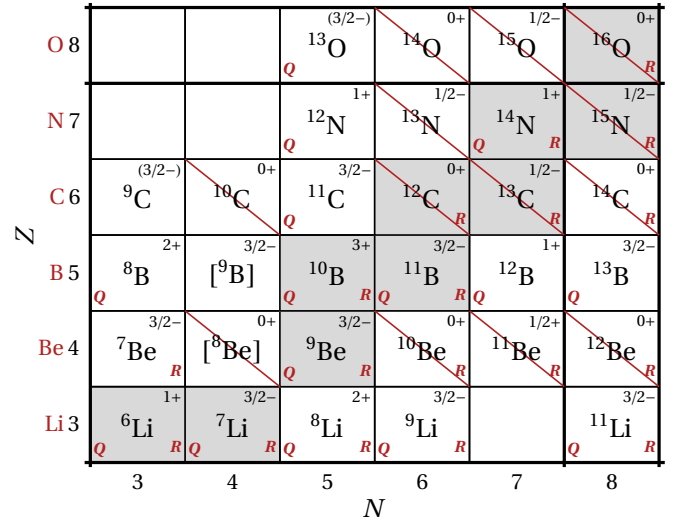


FIG. 1. Overview of particle-bound nuclides in the p shell, where those with measured ground-state quadrupole moments [14] and charge radii [17, 18] are indicated by the letter “Q” or “R”, respectively. Brackets indicate a particle-unbound but narrow ($\lesssim 1$ keV) ground-state resonance, shading indicates beta-stable nuclides, and the experimental ground-state angular momentum and parity are given [18–22]. Nuclei for which the ground-state angular momentum does not support a quadrupole moment ($J \leq 1/2$) are crossed out with a diagonal line.

even nuclei, nor for odd-mass nuclei with $J = 1/2$ ground states. (Nuclei not supporting a ground-state quadrupole moment are crossed out with diagonal line in Fig. 1.)

We observe that the convergence of calculated $E2$ matrix elements may also be correlated with the convergence of the calculated electric monopole ($E0$) moment or, equivalently, root mean square (r.m.s.) radius. The known ground-state charge radius is, like the quadrupole moment, precisely measured in many nuclei [17] (again, as summarized for p -shell nuclei in Fig. 1). Thus, the measured ground-state charge radius, like the quadrupole moment, may be used as a calibration reference, permitting $E2$ transition strengths to be estimated based on robust *ab initio* NCCI predictions for ratios of the form $B(E2)/(e^2r^4)$, without being subject to any constraint on the ground-state angular momentum. However, of course, the determination of either the ground-state quadrupole moment or radius is subject to practical experimental considerations [23, 24], including typically that the nucleus be particle bound.

Similarly, robust *ab initio* NCCI predictions for ratios of the form Q/r^2 permit estimation of the ground-state (or an excited-state) quadrupole moment from a measured radius, or *vice versa*. Only for ${}^7\text{Be}$, among p -shell nuclei, is the radius known but quadrupole moment unknown. However, for the proton-rich nuclides ${}^8\text{B}$, ${}^{11}\text{C}$, and ${}^{12}\text{N}$, as well as neutron-rich ${}^{12}\text{B}$, the quadrupole moment is known while the radius is unknown, as seen from Fig. 1.

Such ratios Q/r^2 also provide *ab initio* insight into the quadrupole deformation. Namely, in an axially symmetric rotational picture, they provide a measure of the Bohr deformation variable β [25] or, more precisely, its microscopically defined counterpart obtained through the quadrupole tensor [26]. We may consider such ratios not only for the proton observables Q_p and r_p , thus providing a measure of the quadrupole deformation β_p for the proton distribution, but also for the corresponding neutron observables Q_n and r_n , thus providing a measure of the quadrupole deformation β_n of the neutron distribution. Although the proton observables are more readily accessible to experiment, through electromagnetic probes, reaction observables are sensitive to the neutron observables (*e.g.*, Refs. [27–30]), at least in a model-dependent fashion. Moreover, parity nonconservation effects in atomic of molecular systems are sensitive to the nuclear weak charge distribution, and thus can provide an alternative means of probing these neutron observables [31, 32].

In the present article (Part I), we focus on the *ab initio* prediction of Q/r^2 , while calibration of *ab initio* predictions for $E2$ strengths to the charge radius is the subject of a subsequent article (Part II) [33]. We first lay out the expected relations between $E2$ and radius observables, in terms of dimensionless ratios (Sec. II A). We also briefly review the conversion between the experimentally accessible charge radius r_c and the point-proton radius r_p that more naturally arises in nuclear structure calculations (Sec. II B) and comment on the physical inter-

pretation of the dimensionless ratio Q/r^2 in terms of the nuclear quadrupole deformation (Sec. II C). We then explore the convergence obtained for the ratio, and compare the resulting predictions against experiment. We first take ${}^9\text{Be}$ as an illustrative case for detailed exploration (Sec. III), including an examination of convergence diagnostics and a straightforward exponential basis extrapolation (for which relations are provided in Appendix A). We then consider the dimensionless ratio Q/r_p^2 for the ground states of particle-bound nuclides across the p shell (Sec. IV). We restrict attention to doubly open-shell nuclei (*i.e.*, with $3 \leq Z, N \leq 7$), since, in the semimagic nuclei (at the $N, Z = 8$ shell closure), mixing with intruder configurations [28, 34] complicates the identification between calculated and physical ground states and disrupts the ordinary convergence patterns [13, 35]. Finally, we translate these results into an exploration of the evolution of the deformations of the proton and neutron distributions within the nuclear ground state, under the assumption of axial symmetry (Sec. V). Preliminary results were reported in Ref. [36].

II. BACKGROUND: DIMENSIONLESS RATIOS OF OBSERVABLES AND THEIR INTERPRETATION

A. Dimensionless ratios

Electric quadrupole moments and $E2$ strengths both may be expressed¹ in terms of reduced matrix elements of the $E2$ operator, $Q_{2\mu} = \sum_{i \in p} e r_i^2 Y_{2\mu}(\hat{\mathbf{r}}_i)$, where the summation runs over the (charged) protons.² Ratios of the form

$$\frac{B(E2)}{(eQ)^2} \propto \left| \frac{\langle \cdots \| \sum_{i \in p} r_i^2 Y_2(\hat{\mathbf{r}}_i) \| \cdots \rangle}{\langle \cdots \| \sum_{i \in p} r_i^2 Y_2(\hat{\mathbf{r}}_i) \| \cdots \rangle} \right|^2 \quad (1)$$

are dimensionless and involve like powers of $E2$ reduced matrix elements (albeit involving different states) in the numerator and the denominator, much as in ratios of quadrupole moments or in ratios of $E2$ strengths. Truncation errors may cancel in such ratios, as explored and exploited in Refs. [8, 15]. In this case, a known ground-state quadrupole moment provides a calibration reference for the $E2$ strength.

¹ The quadrupole moment for a state of angular momentum J is defined [37] in terms of a stretched $E2$ matrix element, as $eQ(J) \equiv (16\pi/5)^{1/2} \langle JJ|Q_{20}|JJ \rangle$, and thus may be written, by the Wigner-Eckart theorem [38, 39], in terms of a reduced matrix element as $eQ(J) = (16\pi/5)^{1/2} (2J+1)^{-1/2} \langle JJ20|JJ \rangle \langle J||Q_2||J \rangle$. The reduced transition probability between states of angular momentum J_i and J_f is likewise expressed in terms of a reduced matrix element as $B(E2; J_i \rightarrow J_f) = (2J_i + 1)^{-1} |\langle J_f||Q_2||J_i \rangle|^2$.

² The $E2$ operator of interest is, more precisely, defined thusly in terms of the *intrinsic* coordinates, taken relative to the nuclear center of mass frame [40].

The r.m.s. point-proton radius r_p is evaluated in terms of the monopole moment $M_0 = \langle J | \sum_{i \in p} r_i^2 | J \rangle$ as $r_p = (M_0/Z)^{1/2}$. Thus, r_p^2 is proportional to a matrix element of a one-body operator, the $E0$ operator, which once again involves an r^2 radial dependence. Ratios Q/r_p^2 or $B(E2)/(e^2 r_p^4)$ involving an $E2$ observable and the appropriate power of r_p are again dimensionless, and involve ratios of similar powers of matrix elements of operators sharing the same r^2 dependence. Namely, these ratios are of the form

$$\frac{Q}{r_p^2} \propto \frac{\langle \dots \| \sum_{i \in p} r_i^2 Y_2(\hat{\mathbf{r}}_i) \| \dots \rangle}{\langle \dots \| \sum_{i \in p} r_i^2 \| \dots \rangle} \quad (2)$$

and

$$\frac{B(E2)}{(e^2 r_p^4)} \propto \left| \frac{\langle \dots \| \sum_{i \in p} r_i^2 Y_2(\hat{\mathbf{r}}_i) \| \dots \rangle}{\langle \dots \| \sum_{i \in p} r_i^2 \| \dots \rangle} \right|^2, \quad (3)$$

respectively. It is not unreasonable to anticipate that errors might again cancel in the ratio. In this case, a known point-proton radius provides a calibration reference for the $E2$ moment or strength.

B. Relation of point-proton and charge radii

To connect with experiment, we must relate the point-proton radius r_p appearing in nuclear structure calculations to the charge radius r_c probed in experiment. At leading order in the inverse nucleon mass, the relationship is expressed as a set of additive corrections to r_p^2 [41–45]:

$$r_c^2 = r_p^2 + \left(\frac{3}{4M_p^2} + R_p^2 \right) + \frac{N}{Z} R_n^2 + r_{\text{s.o.}}^2 + r_{\text{m.e.c.}}^2, \quad (4)$$

where the meanings of the terms on the right hand side are discussed below.

The first two correction terms relative to r_p^2 , in (4), reflect the charge distributions within the nucleons themselves, and are independent of nuclear structure. The term in parentheses accounts for the mean-square charge radius of the proton, which is customarily separated into a Darwin-Foldy contribution [$3/(4M_p^2) = 0.033 \text{ fm}^2$, where M_p is the proton mass], representing the finite charge radius which would be generated due to relativistic effects even for a point proton, and a remaining contribution, taken to represent the effect of the non-pointlike hadronic structure of the proton. It is this latter contribution which is conventionally tabulated as the mean-square charge radius of the proton (denoted in the hadronic physics literature again by r_p^2 [46], but renamed in the nuclear physics literature, *e.g.*, to R_p^2 [45], to avoid overloading the use of r_p in the nuclear sense as defined above in Sec. II A). The R_n^2 term similarly accounts for the mean-square charge radius of the neutron, which reflects the inhomogeneous charge distribution arising within the (overall neutral) neutron. In the present

work, we use $R_p = 0.8409(4) \text{ fm}^2$ [giving $R_p^2 + 3/(4M_p^2) = 0.7401(7) \text{ fm}^2$] and $R_n^2 = -0.1155(17) \text{ fm}^2$ [46].

The remaining two terms represent the relativistic spin-orbit effect (which may be interpreted as a contribution to the charge density arising from Lorentz transformation of the nucleon anomalous magnetic moments) and meson exchange contributions. Their contributions depend in detail upon the nuclear structure and, in the latter case, upon the assumed form of the meson exchange contributions to the charge operator [47–49]. (See Ref. [50] for estimates of the spin-orbit correction.) The corrections in their entirety may in principle be obtained from a chiral effective field theory (χ EFT) expansion, yielding two-body and higher contributions. When extracting values for r_p from the measured r_c [17], in the present work, we only account for the first two correction terms in (4), while neglecting the remaining (structure-dependent and less well-constrained) terms. Nonetheless, it is important to keep in mind their possible relevance.

C. Relation to deformation

The dimensionless ratios considered above, in Sec. II A, are of interest not only for their prospective convergence properties, but also for their physical significance, in the context of rotation and deformation. Ratios of $E2$ matrix elements are a direct prediction of rotational models and depend only upon the nature of the rotation (*e.g.*, axial or triaxial), not directly on the overall magnitude of the deformation. For an axially symmetric rotor [51], all $E2$ matrix elements within a rotational band are proportional to the same intrinsic quadrupole moment

$$eQ_0 \equiv \left(\frac{16\pi}{5} \right)^{1/2} \langle \phi_K | Q_{2,0} | \phi_K \rangle, \quad (5)$$

and the ratio $B(E2)/(eQ)^2$, of (1), for a transition strength and quadrupole moment within the same rotational band, is given simply in terms of Clebsch-Gordan coefficients.³ In contrast, the ratio of an $E2$ matrix element to the monopole moment depends upon the structure of the rotational intrinsic state and provides a measure of the overall magnitude of the deformation. In particular, the axially symmetric rotational picture directly relates the ratios Q/r_p^2 and $B(E2)/(e^2 r_p^4)$, appearing in (2) and (3), to the β deformation of the rotational intrinsic state.

³ For an axially symmetric rotor, within a rotational band with angular momentum projection K along the intrinsic symmetry axis, and rotational intrinsic state $|\phi_K\rangle$, $E2$ reduced matrix elements are given in terms of the intrinsic quadrupole moment Q_0 by $\langle K J_f || Q_2 || K J_i \rangle = [5/(16\pi)]^{1/2} \hat{J}_i(J_i K 2 0 | J_f K) eQ_0$, where $\hat{J} \equiv (2J+1)^{1/2}$, although it should be noted that an additional cross term may contribute for $1/2 \leq K \leq 1$ [51] (see, *e.g.*, Sec. II C of Ref. [9] for reference plots and a summary of the relevant relations).

The Bohr deformation variable β is traditionally introduced in a purely macroscopic context. In terms of the quadrupole ($\lambda = 2$) surface deformation parameters $\alpha_{2\mu}$ appearing in the multipole expansion $R(\theta, \phi) = R_0[1 + \sum_{\lambda\mu} \alpha_{\lambda\mu}^* Y_{\lambda\mu}(\theta, \phi)]$ for the surface displacement of a deformed liquid drop, β is defined as the spherical tensor norm of α_2 , via [25, 52]

$$\beta^2 \equiv \sum_{\mu} |\alpha_{2\mu}|^2. \quad (6)$$

This relation assumes a well-defined nuclear shape, but the deformation need not be axially symmetric (*i.e.*, it may be triaxial).

In microscopic nuclear theory, we work in terms of the quadrupole tensor, rather than surface deformation parameters. In making the connection to the liquid drop picture, it is traditional to consider the *matter* (or point-nucleon) quadrupole tensor rather than the *electromagnetic* (or point-proton) quadrupole tensor of Sec. II A, and to work in terms of the quadrupole moment operator $Q_{2\mu}^{\text{mom}}$ normalized with a conventional factor of $(16\pi/5)^{1/2}$ (see, *e.g.*, footnote 8 of Ref. [40]). Then, the integral expression for the quadrupole tensor in terms of the matter density $\rho(\mathbf{r})$ is $Q_{2\mu}^{\text{mom}} = (16\pi/5)^{1/2} \int r^2 Y_{2\mu}(\hat{\mathbf{r}}) \rho(\mathbf{r}) d^3\mathbf{r}$, and the microscopic representation (in terms of point nucleons) is

$$Q_{2\mu}^{\text{mom}} = \left(\frac{16\pi}{5}\right)^{1/2} \sum_{i \in p, n} e r_i^2 Y_{2\mu}(\hat{\mathbf{r}}_i). \quad (7)$$

In a liquid drop picture, it is straightforward to deduce a relation, valid at leading order in the $\alpha_{2\mu}$, between the components $Q_{2\mu}^{\text{mom}}$ of the quadrupole tensor and the deformation parameters $\alpha_{2\mu}$. This relation involves also the monopole moment (or radius). Namely (see, *e.g.*, Sec. 3.1 of Ref. [26]),

$$Q_{2\mu}^{\text{mom}} = \left(\frac{5}{\pi}\right)^{1/2} M_0 \alpha_{2\mu}. \quad (8)$$

Here, the *matter* monopole moment $M_0 = \int r^2 \rho(\mathbf{r}) d^3\mathbf{r}$, is represented in terms of point nucleons as $M_0 = \sum_{i \in p, n} r_i^2$.

The squared norm of the quadrupole tensor,

$$Q_0^2 \equiv \sum_{\mu} |Q_{2\mu}^{\text{mom}}|^2, \quad (9)$$

is rotationally invariant and thus, in a rotational picture, a property of the rotational intrinsic state (and the same for all members of a rotational band). From the componentwise relation (8) between the tensors $Q_{2\mu}^{\text{mom}}$ and α_2 , their norms Q_0 and β are similarly related as

$$Q_0 = \left(\frac{5}{\pi}\right)^{1/2} M_0 \beta. \quad (10)$$

We may now discard any reference to a classical liquid drop, and take the relation (10) to be a fully microscopic

defining expression for β . Equivalently, in terms of the r.m.s. matter radius r , defined by $M_0 = Ar^2$,

$$Q_0 = \left(\frac{5}{\pi}\right)^{1/2} Ar^2 \beta. \quad (11)$$

Now let us return to electromagnetic (proton) observables, obtained with the proton quadrupole operator of Sec. II A. With replacements $r \rightarrow r_p$, $A \rightarrow Z$, and $\beta \rightarrow \beta_p$ in (11), we obtain

$$Q_0 = \left(\frac{5}{\pi}\right)^{1/2} Z r_p^2 \beta_p. \quad (12)$$

Similar relations may, of course, be written for neutron quadrupole observables, with analogous replacements $r \rightarrow r_n$, $A \rightarrow N$, and $\beta \rightarrow \beta_n$.

To relate the deformation to the laboratory-frame (spectroscopic) observables, we must return to the assumption of axially symmetric rotation. Then the quantity Q_0 of (9) is, to within sign,⁴ none other than the intrinsic quadrupole moment appearing in (5). It is therefore simply related to the rotational $E2$ observables via Clebsch-Gordan coefficients (more general relations can be deduced for triaxial [53] or SU(3) [54] rotation).

We may connect the proton deformation β_p directly with the dimensionless ratio Q/r^2 , for spectroscopic quadrupole moments $Q(J)$, by taking (12) in combination with the definition of the quadrupole moment (footnote 1) and the rotational relations (footnote 3), to obtain

$$\beta_p = \frac{(J+1)(2J+3)}{3K^2 - J(J+1)} \left(\frac{\pi}{5}\right)^{1/2} \frac{Q(J)}{Z r_p^2}. \quad (13)$$

Thus, *e.g.*, for a $K = 3/2$ band head, $\beta_p = \sqrt{5\pi} Q(3/2)/(Z r_p^2)$; for the $J = 3/2$ member of a $K = 1/2$ band, $\beta_p = -\sqrt{5\pi} Q(3/2)/(Z r_p^2)$; or, for the $J = 2$ member of a $K = 0$ band, $\beta_p = -[7\sqrt{\pi}/(2\sqrt{5})] Q(2)/(Z r_p^2)$.

Analogous relations may be derived for $B(E2)/(e^2 r_p^4)$. Specifically, the $0 \rightarrow 2$ (upward) transition strength within a $K = 0$ band is commonly used [55, 56] as a phenomenological measure of deformation [note $B(E2; 0 \rightarrow 2)/B(E2; 2 \rightarrow 0) = 5$]. From (12), we have

$$\beta_p = \frac{4\pi}{5} \frac{B(E2; 0 \rightarrow 2)^{1/2}}{Z e r_p^2}. \quad (14)$$

By comparison, the traditional expression

$$\beta = \frac{4\pi}{3} \frac{B(E2; 0 \rightarrow 2)^{1/2}}{Z e r_0^2 A^{2/3}}, \quad (15)$$

⁴ The quantities β and Q_0 are interpreted, in (6) and (9), respectively, as the unsigned norms of spherical tensors. However, the intrinsic quadrupole moment Q_0 of (5) is a signed matrix element, where a positive value, in a liquid drop picture, indicates prolate deformation and a negative value oblate deformation.

used in Refs. [55, 56], is obtained from (14) if, instead of using the actual nuclear radius, one adopts a global phenomenological estimate $r = (3/5)^{1/2} r_0 A^{1/3}$ for the nuclear r.m.s. radius. One must, furthermore, suppose that charge is homogeneously distributed within the nuclear matter, so that r_p may be taken to be simply given by r . Such assumptions are, however, to be regarded with extreme caution for light nuclei.

III. CONVERGENCE ILLUSTRATION: ${}^9\text{Be}$

As an illustrative example, let us first take the $3/2^-$ ground state of ${}^9\text{Be}$. The ground state charge radius and quadrupole moment are both known experimentally (Fig. 1).

The calculated ground state observables are shown in Fig. 2. Calculations are carried out using the NCCI code MFDn [58]. The basis for an NCCI calculation must be restricted to finite size, by truncation to configurations with some maximum number N_{max} of oscillator excitations (taken relative to the lowest Pauli-allowed filling of oscillator shells) [7]. Results converge towards the true result (that is, as it would be obtained from solution of the many-body problem in the full, untruncated many-body space) with increasing N_{max} . Each curve in Fig. 2 represents the results of calculations sharing the same N_{max} , but with varying choices of the oscillator parameter $\hbar\omega$, which determines the oscillator length $b \propto (\hbar\omega)^{-1/2}$ [37], for the basis functions. (Results are shown for $4 \leq N_{\text{max}} \leq 12$ and $10 \text{ MeV} \leq \hbar\omega \leq 30 \text{ MeV}$.) In general, an approach to convergence is signaled by calculated values which no longer change with increasing N_{max} (compression of successive curves) and are locally insensitive to the choice of oscillator parameter (flatness with respect to $\hbar\omega$). Computational resources limit the N_{max} for which calculations are feasible and thus the precision which can be obtained.

For purposes of comparison, we take NCCI calculations based on three different internucleon interactions (left to right in Fig. 2): Daejeon16 [59], JISP16 [60], and a LENPIC chiral effective field theory (χEFT) interaction [61, 62]. Of these interactions, Daejeon16 is the “softest”, providing the most favorable convergence properties. It was obtained as the two-body part of an N^3LO χEFT interaction [63], but was then softened via a similarity renormalization group (SRG) transformation [64] so as to provide comparatively rapid convergence (and subsequently adjusted via a phase-shift equivalent transformation to better describe nuclei with $A \leq 16$ without requiring the introduction of a three-body contribution). In contrast, the “hardest” is the LENPIC interaction, which, for purposes of illustration, is taken here as a bare interaction, with no SRG softening (specifically, we use the two-body N^2LO interaction with $R = 1 \text{ fm}$ semi-local coordinate-space regulator [61, 62]).

The difference in hardness of these interactions is readily apparent in the calculated ground state energies, for

which the convergence behavior is shown in Fig. 2 (top). In each case, the calculated ground state energy for a given fixed N_{max} has a variational minimum at some $\hbar\omega$, ranging from $\hbar\omega \approx 15 \text{ MeV}$ for Daejeon16 [Fig. 2(a)] to $\hbar\omega \lesssim 30 \text{ MeV}$ for LENPIC [Fig. 2(c)]. The results for Daejeon16 display a robust approach to convergence, at the level of $\lesssim 0.1 \text{ MeV}$ (for $\hbar\omega$ near the variational minimum), while the results for LENPIC [Fig. 2(c)] still differ by $\approx 5 \text{ MeV}$ for the highest two N_{max} values shown.

Let us focus first on the results obtained with the Daejeon16 interaction, for which the calculated quadrupole moment is shown in Fig. 2(d). These results show tendencies towards convergence. We can see a flattening (shouldering) of the curves, in the lower portion of the $\hbar\omega$ range shown, and the spacing between curves for successive N_{max} decreases modestly. It would not be unreasonable to estimate the calculations to be converging towards something close to the experimental value (square). However, the convergence is not sufficiently developed for us to read off a concrete estimate of the true result for the full, untruncated space. Although the curves appear to approximately cross at a single point at the low end of the $\hbar\omega$ range shown, and it has been suggested [2] that such a crossing point may be taken to provide a heuristic estimate for the true, converged value, such estimates are not necessarily found to be robust [65].

Taking now the calculated point-proton radius, shown in Fig. 2(g), the $\hbar\omega$ dependence is superficially less pronounced than for the quadrupole moment [Fig. 2(d)]. However, recall that the radius goes as the square root of the matrix element of an operator with r^2 radial dependence, while the quadrupole moment is simply proportional to such a matrix element, and higher powers amplify relative changes (in this case, by a factor of 2). For both observables, the values must rise towards infinity at sufficiently low $\hbar\omega$ and must fall towards zero at sufficiently large $\hbar\omega$, in a finite oscillator basis, since the oscillator functions only provide support at a radial distance scale in the vicinity of the oscillator length [$b \propto (\hbar\omega)^{-1/2}$]. The curves representing the radius for different N_{max} have a crossing point somewhat higher in $\hbar\omega$ (by $\approx 2.5 \text{ MeV}$) than for the quadrupole moment. This makes it clear that the calculated Q and r_p^2 cannot be strictly correlated, across different N_{max} and $\hbar\omega$, as they would have to be in order to yield a truly constant value for the dimensionless ratio Q/r_p^2 .

Nonetheless, taking the dimensionless ratio Q/r_p^2 , as shown in Fig. 2(j), serves to eliminate much of the $\hbar\omega$ dependence found in the calculated quadrupole moment. Moreover, it would appear to improve convergence with respect to N_{max} . It may be noted that the ratio Q/r_p^2 is monotonically increasing with N_{max} , with no crossings of curves for successive N_{max} , over the $\hbar\omega$ range shown.

Such observations may be made more quantitative by considering the *differences* in the calculated values, for successive N_{max} , yielding diagnostics of the convergence such as those shown (for these Daejeon16 results) in Fig. 3. For an observable $X(N_{\text{max}})$, at fixed $\hbar\omega$, we

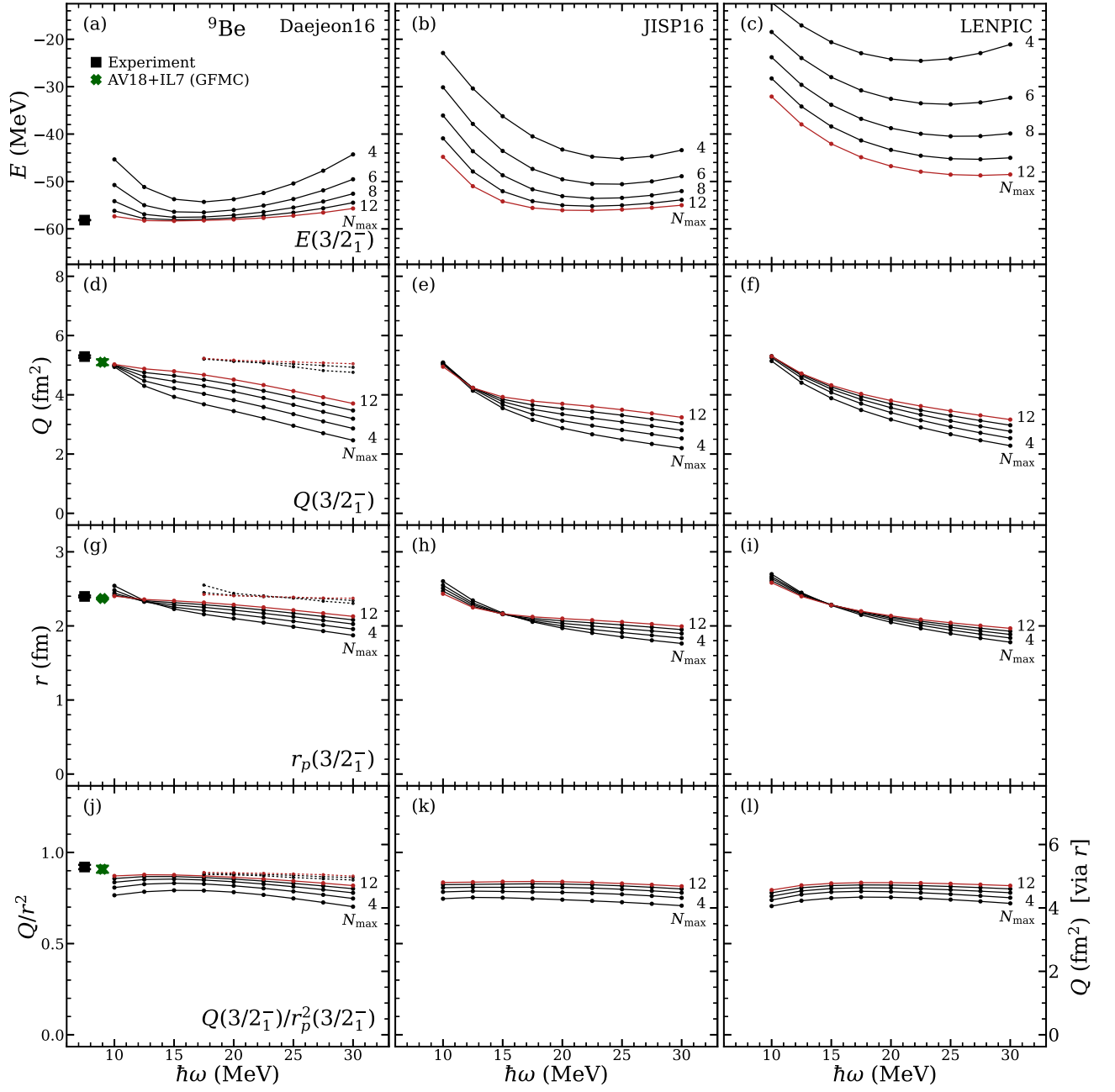


FIG. 2. Calculated ground state observables for ${}^9\text{Be}$: $E(3/2_1^-)$ (top), $Q(3/2_1^-)$ (upper middle), $r_p(3/2_1^-)$ (lower middle), and the dimensionless ratio Q/r_p^2 constructed from the preceding two observables (bottom). Results are shown for the Daejeon16 (left), JISP16 (center), and LENPIC (right) interactions. Calculated values are shown as functions of the basis parameter $\hbar\omega$, for successive even values of N_{max} , from $N_{\text{max}} = 4$ to 12 (as labeled). When calibrated to the experimentally deduced value for r_p , the ratio provides a prediction for the absolute Q (scale at right). Exponential extrapolations (small circles, dotted lines) are provided, for the Daejeon16 results only ($\hbar\omega \geq 17.5$ MeV). For comparison, experimental values [14, 17, 20] (squares) and GFMC AV18+IL7 predictions [57] (crosses) are also shown.

consider the relative difference (or logarithmic difference) $\Delta_{\text{rel}}[X]$ [Fig. 3 (left)], which we define by

$$\Delta_{\text{rel}}[X](N_{\text{max}}) = \frac{X(N_{\text{max}}) - X(N_{\text{max}} - 2)}{\frac{1}{2}[X(N_{\text{max}}) + X(N_{\text{max}} - 2)]}. \quad (16)$$

We also consider the ratio of successive differences [66],

$$\eta[X](N_{\text{max}}) \equiv \frac{X(N_{\text{max}}) - X(N_{\text{max}} - 2)}{X(N_{\text{max}} - 2) - X(N_{\text{max}} - 4)}, \quad (17)$$

which measures how rapidly the step size, between values for the observable for successive N_{max} , decreases with increasing N_{max} .

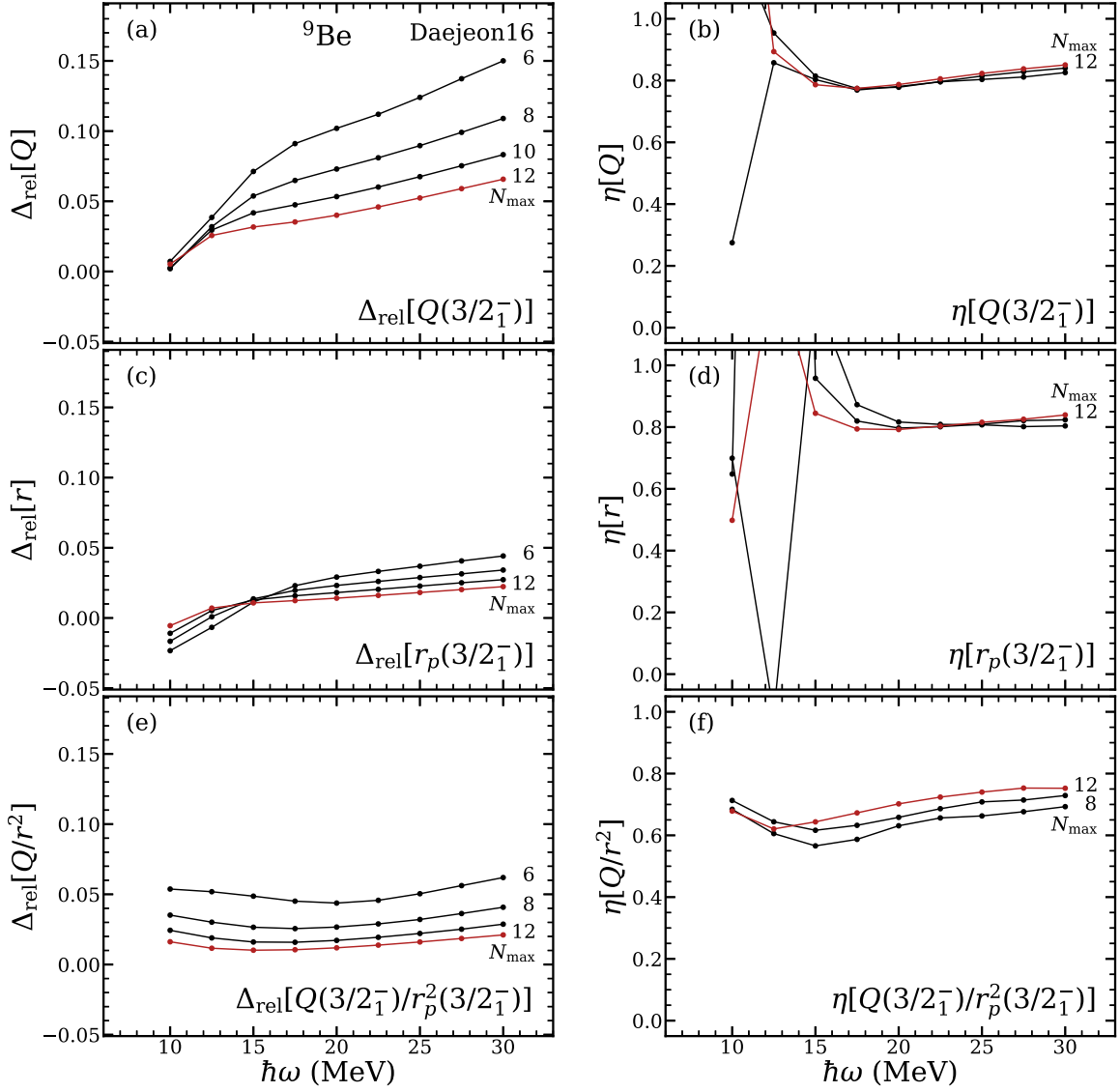


FIG. 3. Diagnostics of convergence for ground state observables for ${}^9\text{Be}$: the relative difference Δ_{rel} (left) and ratio of successive differences η (right), for $Q(3/2^-_1)$ (top), $r_p(3/2^-_1)$ (middle), and the dimensionless ratio Q/r_p^2 (bottom). Calculated values, for the Daejeon16 interaction, are shown as functions of the basis parameter $\hbar\omega$, for successive even values of N_{max} , from $N_{\text{max}} = 4$ to 12 (as labeled).

If one assumes exponential convergence with respect to N_{max} [2, 67], of the form

$$X(N_{\text{max}}) = X_{\infty} + a \exp(-cN_{\text{max}}), \quad (18)$$

then the limiting value X_{∞} is approached (as $N_{\text{max}} \rightarrow \infty$) in steps with sizes which form a geometric progression, and the ratio of successive differences is simply a constant $\eta[X] = e^{-2c}$, independent of N_{max} . Conversely, constant η indicates exponential convergence. Some observations regarding this geometric progression, relevant to carrying out a three-point exponential extrapolation, may be found in Appendix A.

For the quadrupole moment itself, the relative differences $\Delta_{\text{rel}}[Q]$ [Fig. 3(a)] essentially vanish ($\lesssim 1\%$) at the low end of the $\hbar\omega$ range shown, where the curves for Q

[Fig. 2(d)] are crossing. Taking $\hbar\omega = 20$ MeV as a more illustrative point for comparison, the relative differences decrease from $\approx 10\%$ at $N_{\text{max}} = 6$ to $\approx 4\%$ at $N_{\text{max}} = 12$. For the radius, the relative differences $\Delta_{\text{rel}}[r_p]$ [Fig. 3(c)] range from $\approx 3\%$ at $N_{\text{max}} = 6$ to $\approx 1.4\%$ at $N_{\text{max}} = 12$, again for $\hbar\omega = 20$ MeV, reflecting both the different $\hbar\omega$ at which the curves cross [Fig. 2(g)] and a smaller overall scale of differences. At least in the region of larger $\hbar\omega$, to the right of any crossing points, the ratios of successive differences, $\eta[Q]$ [Fig. 3(b)] and $\eta[r_p]$ [Fig. 3(d)], demonstrate that the convergence is approximately exponential for both the quadrupole moment and radius, with a ratio $\eta \approx 0.8$ for successive steps, or an $\approx 20\%$ reduction in size for successive steps. This implies that the distance remaining to the limiting value is ≈ 4 times the size of

the last step taken (see Appendix A). This ratio, and thus the decay constant c , is only weakly dependent on $\hbar\omega$, increasing to ≈ 0.85 by $\hbar\omega = 30$ MeV.

Then, for the ratio the relative differences $\Delta_{\text{rel}}[Q/r_p^2]$ [Fig. 3(e)] are relatively independent of $\hbar\omega$, decreasing from $\approx 4\%$ at $N_{\text{max}} = 6$ to $\approx 1.2\%$ at $N_{\text{max}} = 12$, much smaller than for the quadrupole moment itself over most of the $\hbar\omega$ range [Fig. 3(a)]. The ratios $\eta[Q/r_p^2]$ of successive differences [Fig. 3(f)] indicate that the convergence pattern for Q/r_p^2 is less purely exponential in N_{max} , as η varies significantly with N_{max} , increasing from ≈ 0.6 to ≈ 0.7 over the three steps in N_{max} shown. Indeed, the ratio of two exponentially converging quantities is not itself, in general, expected to be exponentially converging, although it may be approximately so in limiting cases.

Returning to the other interactions in Fig. 2, any indication of shouldering in the calculated quadrupole moment is less visible for JISP16 [Fig. 2(e)] and especially for the bare LENPIC interaction [Fig. 2(f)]. The successive differences in the calculated quadrupole moment do decrease in size (in fact, the convergence for JISP16 is again remarkably exponential in N_{max} , with $\eta \approx 0.8$). But, again, we would be hard put to read off a concrete estimate of the true result. Nonetheless, even for these harder interactions, taking the dimensionless ratio Q/r_p^2 [Fig. 2(k,l)] once again serves to eliminate much of the $\hbar\omega$ dependence found in the calculated quadrupole moment.

Moreover, for the three choices of interaction considered here, the calculated ratios Q/r_p^2 [Fig. 2 (bottom)] are largely indistinguishable. In an axially symmetric rotational description, we may interpret this as a robust prediction for the deformation (Sec. II C), independent of choice of interaction. The calculated ratios, for all three interactions, lie below the experimental ratio (square) but increase towards it from below with increasing N_{max} , such that there is no clear discrepancy between the predictions and experiments. The experimental ratio $Q/r_p^2 \approx 0.92$ yields, via (13), a deformation $\beta_p \approx 0.91$.

While our goal in the present work is not to carry out detailed studies of prospective basis extrapolation schemes (*e.g.*, Ref. [5]), the above observations qualitatively consistency with exponential convergence suggest attempting at least a basic three-point exponential extrapolation with respect to N_{max} (Appendix A). The results of such an extrapolation are shown (small circles, dotted lines), for the ${}^9\text{Be}$ results obtained with the Daejeon16 interaction, for Q [Fig. 2(d)], r_p^2 [Fig. 2(g)], and Q/r_p^2 [Fig. 2(j)]. (From the calculations considered here, which have $N_{\text{max}} \geq 4$, a three-point extrapolation becomes possible for $N_{\text{max}} \geq 8$.) While we cannot compare the extrapolated values to a true, converged result, we may note that the extrapolations are remarkably stable with respect to both N_{max} and $\hbar\omega$, in the region ($\hbar\omega \gtrsim 17.5$ MeV) well above the location of any crossing of the curves, at least for the underlying observables Q [Fig. 2(d)] and r_p^2 [Fig. 2(g)]. Such an extrapolation is less obviously useful for the ratio [Fig. 2(j)], seen above [Fig. 3(f)] to be more rapidly convergent but less expo-

nential in its convergence. Similar extrapolations for the results obtained with the JISP interaction are more erratic, and those obtained with the (bare) LENPIC interactions are essentially unusable. (These extrapolations are not shown in Fig. 2, to avoid obscuring the curves of principal interest, but are available in the Supplemental Material [68].) This difference in success of the extrapolation might be taken to reflect the less converged starting point for extrapolation provided by these harder interactions.

The ground state quadrupole moment is known for ${}^9\text{Be}$, so that here our goal is to provide an experimental test of the predicted ratio, rather than an estimate for an unknown quadrupole moment from a known radius (or *vice versa*). Nonetheless, for illustration, normalizing to the experimental proton radius gives the scale for Q shown at right in Fig. 2 (bottom).

A point of theoretical comparison is provided by the Green's function Monte Carlo (GFMC) [4] approach, which also yields predictions for $E2$ and radius observables for lower p -shell nuclei. The predicted Q and r_p for ${}^9\text{Be}$, from GFMC calculations [57] with the Argonne v_{18} (AV18) two-nucleon [69] and Illinois-7 (IL7) three-nucleon [70] potentials, are shown (crosses) in Fig. 2, along with the deduced ratio Q/r_p^2 [Fig. 2 (bottom)]. In the GFMC results, the dominant uncertainties are statistical in nature, and errors would not *a priori* be expected to cancel in the ratio (although some correlation in errors is possible, especially if the GFMC calculations for different observables are carried out using the same set of Monte Carlo samples). The ratio is only taken here for purposes of comparison. The GFMC predictions for both observables individually lie just below experiment, while the ratio is consistent with experiment to within uncertainties. The NCCI results therefore also appear to be converging towards approximate consistency with the GFMC result for the ratio.

IV. QUADRUPOLE MOMENTS OF p -SHELL NUCLEI

For a concise overview of the *ab initio* results for Q/r_p^2 across the p shell, in Figs. 4 and 5 we restrict our attention to a single, fixed value for the oscillator parameter $\hbar\omega$, and examine the N_{max} dependence of the calculated results. (Here, we take $\hbar\omega = 20$ MeV as a representative value, near the variational energy minima obtained for the Daejeon16 and JISP16 interactions [Fig. 2 (top)].) Results for mirror nuclide pairs are shown in Fig. 4 (with proton-rich nuclei at top, and neutron-rich nuclei at bottom), while results for $N = Z$ nuclei are shown in Fig. 5.⁵ In addition to the ground states of particle-bound p -shell

⁵ The convergence of the quadrupole moment itself may be seen in the Supplemental Material [68]. See also Fig. 4 of Ref. [13].

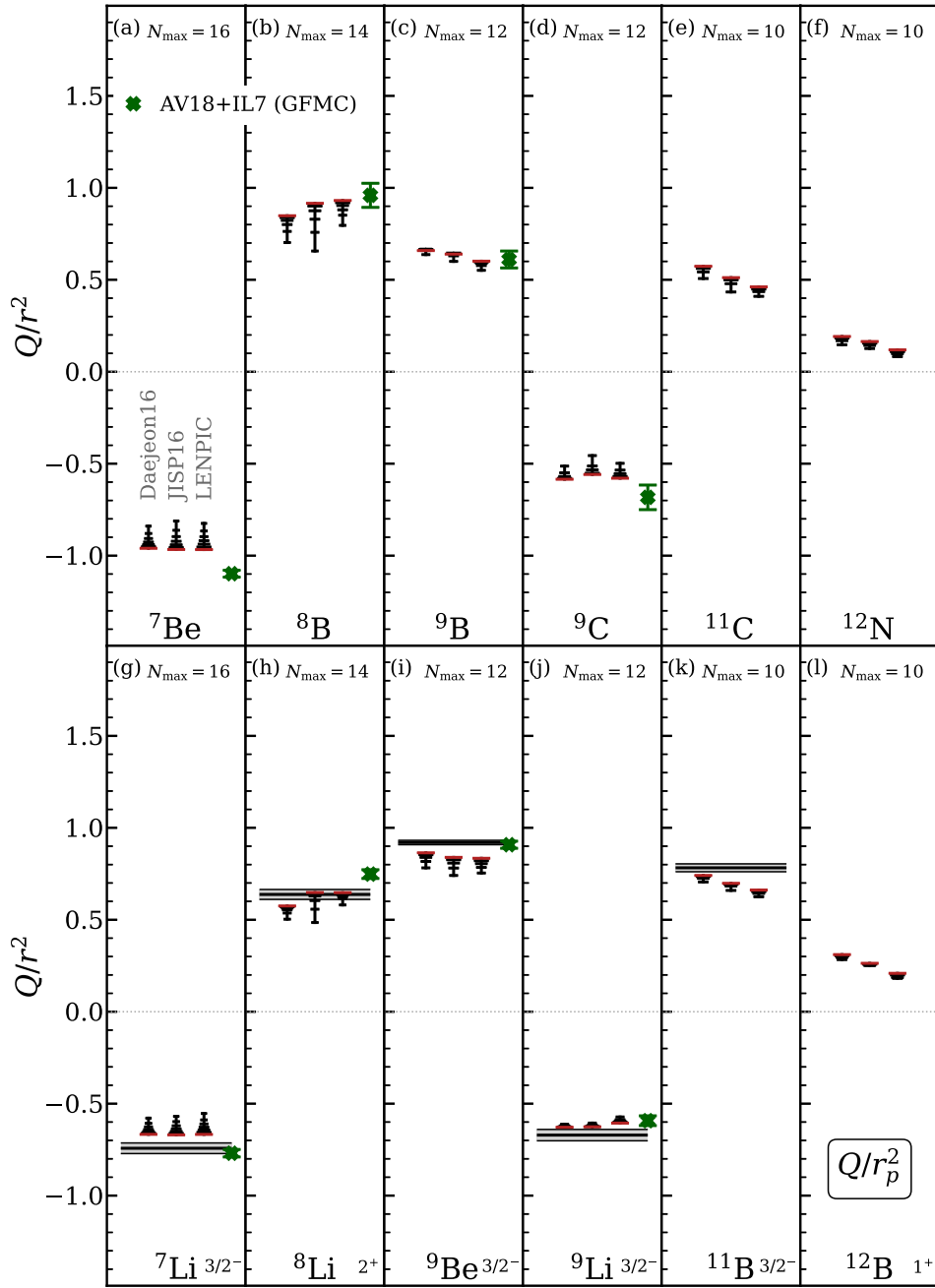


FIG. 4. Calculated ratios Q/r_p^2 , for the ground states of proton-rich (top) and neutron-rich (bottom) nuclides in the p shell, obtained with the Daejeon16, JISP16, and LENPIC interactions (from left to right, within each panel). Calculated values are shown at fixed $\hbar\omega = 20$ MeV and varying N_{\max} (increasing tick size), from $N_{\max} = 4$ to the maximum value indicated (at top). For comparison, the experimental ratios [14, 17] are shown (horizontal line and error band, where the signs of some quadrupole moments are experimentally undetermined), as are the GFMC AV18+IL7 predictions [57, 71] (crosses).

nuclides (with $J \geq 1$), we also include, to complete the set of mirror nuclides, the narrow ground state resonance of ${}^9\text{B}$ [Fig. 4(c)].

Thus, for ${}^9\text{Be}$, the results in Fig. 4(i) represent a vertical slice through the curves shown in Fig. 2 (bottom). Comprehensive plots of the calculated (and extrapolated) observables and ratios, as functions of both N_{\max} and $\hbar\omega$, for both proton and neutron observables, are provided

in the Supplemental Material [68], along with numerical tabulations of the calculated quantities.

Both the quadrupole moment and radius are simultaneously known, yielding an experimental value for the dimensionless ratio, for all the neutron-rich nuclei except ${}^{12}\text{B}$ [Fig. 4 (bottom)], and for the $N = Z$ nuclei (Fig. 5), but not for any of the proton-rich nuclei [Fig. 4 (top)]. The experimental results for the ratio are shown in Figs. 4

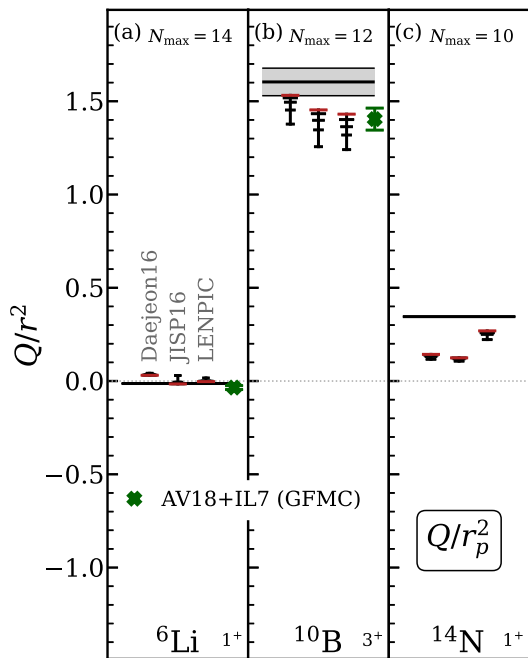


FIG. 5. Calculated ratios Q/r_p^2 , for the ground states of $N = Z$ nuclides in the p shell, obtained with the Daejeon16, JISP16, and LENPIC interactions (from left to right, within each panel). Calculated values are shown at fixed $\hbar\omega = 20$ MeV and varying N_{\max} (increasing tick size), from $N_{\max} = 4$ to the maximum value indicated (at top). For comparison, the experimental ratios [14, 17] are shown (horizontal line and error band, where the signs of some quadrupole moments are experimentally undetermined), as are the GFMCAV18+IL7 predictions [57] (crosses).

and 5 (horizontal lines, with error bands) where available. (The experimental quadrupole moments in these figures are from Ref. [14], except that the value for ^{12}N is corrected as noted in Table I of Ref. [13]. The experimental point-proton radii are deduced, as described in Sec. II B, from the evaluated charge radii of Ref. [17].) The GFMCAV18+IL7 predictions [57, 71], are also shown (crosses), for $A \leq 10$.

We may note some overall features of the calculated ratios Q/r_p^2 (Figs. 4 and 5):

(1) The magnitude of the calculated ratio (that is, regardless of sign) typically converges from below, that is, monotonically increases in N_{\max} , except in the anomalous case of ^6Li [Fig. 5(a)] (discussed below).

(2) Convergence of the calculated ratio tends to be slower for the proton-rich nuclei [Fig. 4 (top)], than for their mirror neutron-rich nuclei [Fig. 4 (bottom)], with the exception of the $^9\text{B}/^9\text{Be}$ mirror pair [Fig. 4(c,i)]. In particular, this difference is seen in the greater spread among the calculated values (or longer “tail” in the plot), from lowest to highest N_{\max} shown.

(3) The predictions for the ratio rarely differ, among the three interactions, by more than ≈ 0.1 , with the exception of ^{14}N [Fig. 5(c)]. However, strict claims cannot be made, given incompletely converged results.

(4) Where the ratio is experimentally known, the calculated ratios are in general agreement with experiment, typically differing by $\lesssim 0.1$ (or at most ≈ 0.2 , for ^{14}N [Fig. 5(c)]) from the experimental central value. If there is an overall tendency, it is that the calculations underpredict the ratio (in magnitude) rather than overpredict. (The difference between the calculated and measured ratio is perhaps most striking for ^7Li [Fig. 4(g)], not for the scale of the disagreement, but since the NCCI results are so consistent across interactions, with differences among themselves much smaller than the difference from experiment.) However, since the calculated values increase (in magnitude) with N_{\max} , this observation may in part be an artifact of incomplete convergence. Furthermore, any differences from experiment should be revisited in the context of the corrections omitted in translating the charge radius to a point-proton radius (Sec. II B), as well as possible meson exchange (or χEFT) corrections to the $E2$ operator used in calculating the quadrupole moment.

(5) The calculated ratios are also in approximate agreement with those from the GFMCAV18+IL7 calculations, again differing by $\lesssim 0.1$, allowing for the statistical uncertainties (shown) in the GFMCAV18+IL7 results. A notable discrepancy is found for the $A = 7$ nuclei [Fig. 4(a,g)] where the NCCI calculations for different interactions are in close agreement with each other (as just noted above for ^7Li), but the GFMCAV18+IL7 result is larger (in magnitude) by ≈ 0.1 . A similar discrepancy is found for ^8Li [Fig. 4(h)], but not the mirror nuclide ^8B [Fig. 4(b)].

Returning to the comparison across mirror nuclei, in the second item above, differences in convergence rate between the neutron-rich nuclei [Fig. 4 (bottom)] and their proton-rich mirror nuclei [Fig. 4 (top)] need not imply any differences in convergence rates for the wave functions *per se*, for these two sets of nuclei. Rather, it must be kept in mind that the observables under consideration probe only the protons. However, the protons are the more tightly bound nucleonic species in the neutron-rich nuclei, but the less tightly bound species in the proton-rich nuclei. Spatially extended halo orbitals or molecular orbitals (*e.g.*, Ref. [72, 73]) for neutrons are expected to be prevalent in neutron-rich nuclei, with mirror symmetry implying that protons are to be found in corresponding spatially extended configurations in proton-rich nuclei (*e.g.*, Ref. [74]).

Indeed, comparing the calculated ratio of neutron observables Q_n/r_n^2 in the neutron-rich nuclei, as shown in Fig. 6, with the corresponding ratio of proton observables for the proton-rich mirror nuclei [Fig. 4 (top)], we see qualitative features which are essentially identical. Thus the main differences in Q/r_p^2 across mirror nuclides (Fig. 4), both in value and in convergence behavior, follow simply from the proton-neutron asymmetry of the structure, while maintaining mirror symmetry.⁶

⁶ Residual quantitative deviations from mirror symmetry do arise,

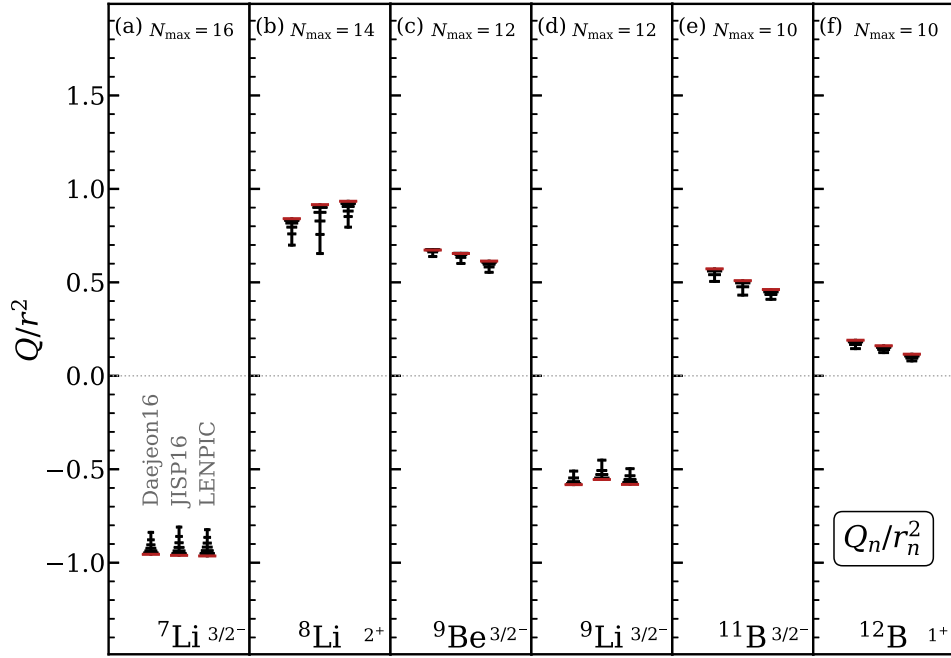


FIG. 6. Calculated ratios Q_n/r_n^2 , involving neutron observables, for the ground states of neutron-rich nuclides in the p shell, obtained with the Daejeon16, JISP16, and LENPIC interactions (from left to right, within each panel). Calculated values are shown at fixed $\hbar\omega = 20$ MeV and varying N_{\max} (increasing tick size), from $N_{\max} = 4$ to the maximum value indicated (at top).

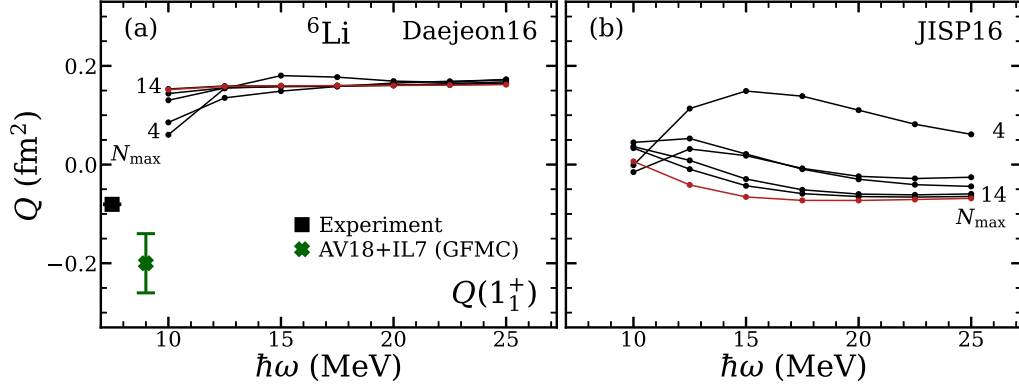


FIG. 7. Calculated ground state quadrupole moment $Q(1_1^+)$ for ${}^6\text{Li}$. Results are shown for the (a) Daejeon16 and (b) JISP16 interactions. Calculated values are shown as functions of the basis parameter $\hbar\omega$, for successive even values of N_{\max} , from $N_{\max} = 4$ to 14 (as labeled). For comparison, the experimental value [14] (square) and GFM AV18+IL7 prediction [57] (cross) are also shown.

The nuclide ${}^6\text{Li}$ [Fig. 5(a)] warrants comment as an exceptional case. The experimental quadrupole moment [$Q(1_1^+) \approx -0.08 \text{ fm}^2$] is an order of magnitude smaller than suggested by the Weisskopf single-particle scale [75] of $\approx 1 \text{ efm}^2$ for $E2$ matrix elements in this mass region, and 1–2 orders of magnitude smaller than the other

measured quadrupole moments for p -shell nuclides [14]. The *ab initio* calculations for the ${}^6\text{Li}$ quadrupole moment have atypical convergence patterns with N_{\max} and $\hbar\omega$, as shown in Fig. 7 for the Daejeon16 and JISP16 interactions. (Convergence of the ${}^6\text{Li}$ quadrupole moment for the JISP16 interaction was explored in detail in Refs. [3, 76].) The NCCI calculated quadrupole moment starts positive at low N_{\max} . The Daejeon16 results [Fig. 7(a)] then rapidly converge to a smaller, but still positive, value of $Q(1_1^+) \approx +0.15 \text{ fm}^2$, while the JISP16 results [Fig. 7(b)] cross zero (as do the even less monotonic LENPIC results, not shown). Changes so large and erratic that they even affect the sign are not the type of

due to effects of the Coulomb interaction in the Daejeon16 and JISP16 calculations, as well as additional strong-interaction components in the LENPIC calculations. The extent to which mirror symmetry is violated in the calculated quadrupole moments is examined in detail in Sec. IV of Ref. [13].

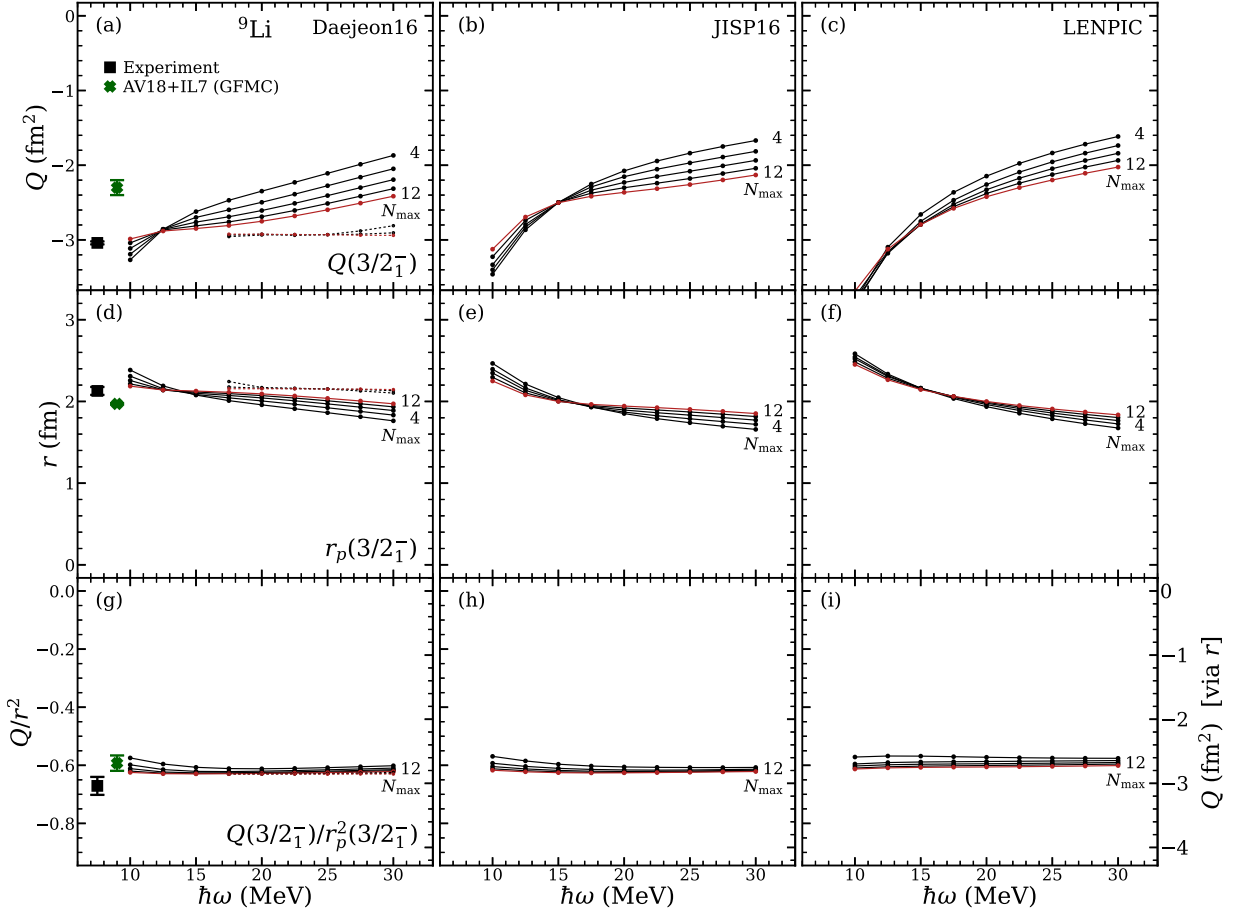


FIG. 8. Calculated ground state observables for ${}^9\text{Li}$: $Q(3/2_1^-)$ (top), $r_p(3/2_1^-)$ (middle), and the dimensionless ratio Q/r_p^2 (bottom). Results are shown for the (left) Daejeon16, (center) JISP16, and (right) LENPIC interactions. Calculated values are shown as functions of the basis parameter $\hbar\omega$, for successive even values of N_{max} , from $N_{\text{max}} = 4$ to 12 (as labeled). When calibrated to the experimentally deduced value for r_p , the ratio provides a prediction for the absolute Q (scale at right). Exponential extrapolations (small circles, dotted lines) are provided, for the Daejeon16 results only ($\hbar\omega \geq 17.5$ MeV). For comparison, experimental values [14, 17] (squares) and GFMC AV18+IL7 predictions [57] (crosses) are also shown.

systematic truncation error which we might hope to offset by simply dividing out the smooth convergence behavior of the squared radius. (The value of the quadrupole moment in ${}^6\text{Li}$, much smaller than the typical single-particle scale, may be understood as arising from cancellations of short-range and long-range contributions in the radial quadrupole density [76], which may also underlie the atypical convergence behavior.) Doing so, as in Fig. 5(a), can have only an incidental effect in ameliorating the irregularities.

Although the convergence for ${}^9\text{Li}$, shown in Fig. 8, is similar to that for ${}^9\text{Be}$ (Fig. 2), further comment is warranted on the magnitude of the quadrupole moment. We again find that taking the dimensionless ratio Q/r_p^2 [Fig. 8 (bottom)] largely eliminates the $\hbar\omega$ dependence, while also improving compression of the results for successive N_{max} . For ${}^9\text{Li}$, the predicted ratio $Q/r_p^2 \approx -0.63$ is again consistent across all three interactions (although somewhat less well converged for LENPIC). These values lie just below (in magnitude) the uncertainties on the ex-

perimental ratio $Q/r_p^2 = -0.67(3)$ [14, 17], and just above the upper end of the statistical uncertainties on the result $Q/r_p^2 = -0.59(3)$ obtained from the GFMC AV18+IL7 calculated quadrupole moment and radius [57].

However, taking the predictions for the quadrupole moment by itself, the GFMC results underpredict experiment (in magnitude) by $\approx 24\%$. In contrast, NCCI calculations with the Daejeon16 interaction [Fig. 2(a)] show strong indications of convergence (in particular, shouldering), as well as a clear crossing point for curves of successive N_{max} , suggesting a quadrupole moment clearly larger in magnitude than for the GFMC AV18+IL7 results and roughly consistent with the experimental result. The simple three-point extrapolations (small circles, dotted lines) are again robust and likewise suggest a value for Q much closer to experiment, underpredicting experiment (in magnitude) by $\lesssim 3\%$, while the extrapolated radius is consistent with experiment [Fig. 2(d)].

Only for ${}^7\text{Be}$, among the p -shell nuclides, is the charge radius measured but quadrupole moment unknown. The

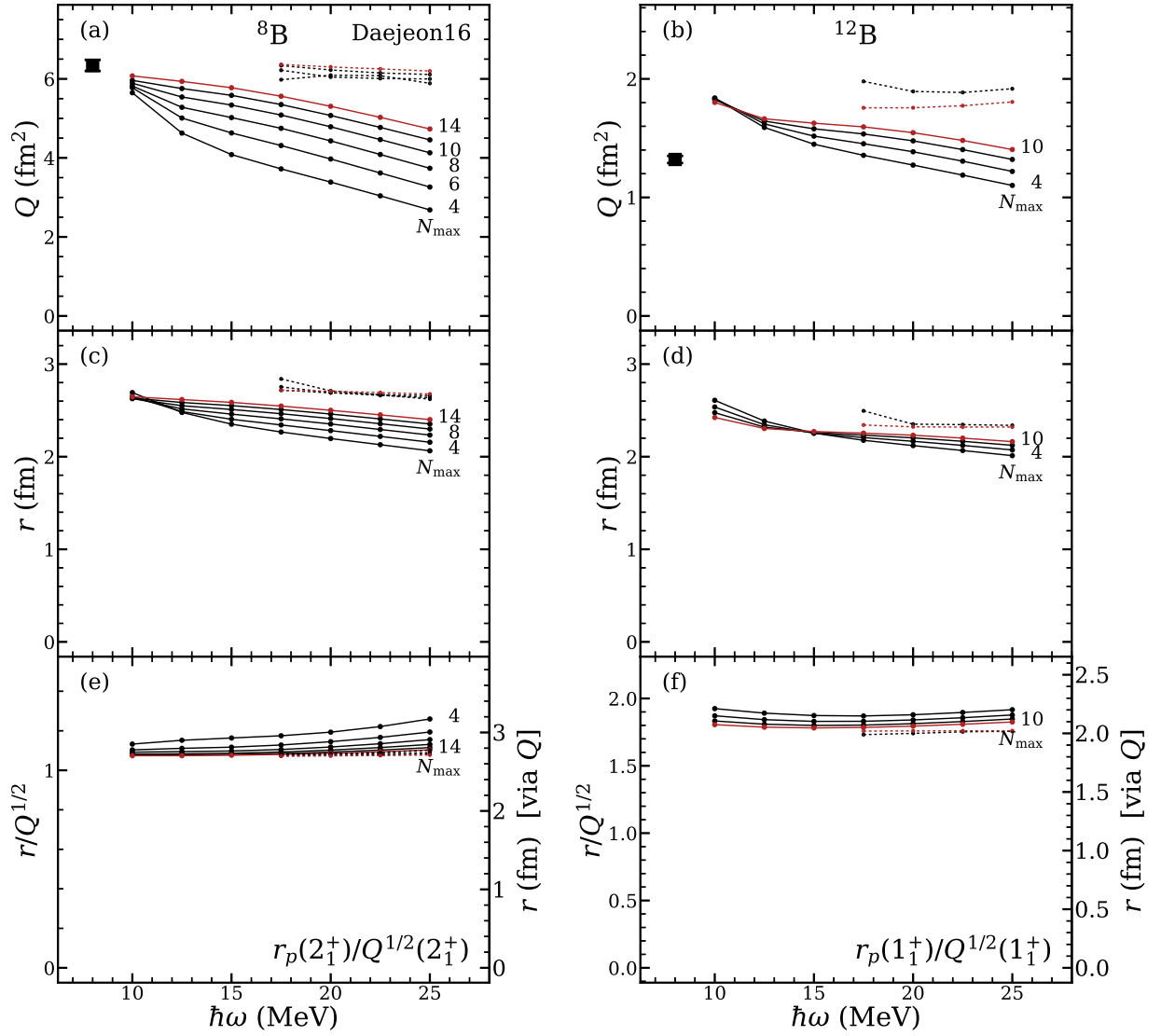


FIG. 9. Calculated observables for the 2^+ ground state of ${}^8\text{B}$ (left) and the 1^+ ground state of ${}^{12}\text{B}$ (right): Q (top), r_p (middle), and the dimensionless ratio $r_p/Q^{1/2}$ (bottom). Results are shown for the Daejeon16 interaction. Calculated values are shown as functions of the basis parameter $\hbar\omega$, for successive even values of N_{\max} , from $N_{\max} = 4$ to the maximum value calculated (as labeled). For comparison, the experimental quadrupole moment [14] is shown (horizontal line and error band). When calibrated to the experimentally deduced value for Q , the ratio provides a prediction for the absolute r_p (scale at right). Exponential extrapolations (small circles, dotted lines) are provided ($\hbar\omega \geq 17.5$ MeV).

calculated Q/r_p^2 [Fig. 4(a)] are rapidly converging with N_{\max} and apparently consistent across interactions, with $Q/r_p^2 \approx -1.0$. The measured charge radius [17] yields a proton radius of $r_p = 2.52(2)$ fm, allowing us to estimate $Q_p \approx -6.3$ fm². However, the apparent systematic discrepancy of the predicted Q/r_p^2 from experiment for the mirror nuclide ${}^7\text{Li}$ [Fig. 4(g)], noted above, might give us pause. In any event, an estimate for the quadrupole moment of ${}^7\text{Be}$ is already available by calibration to another $E2$ observable, the quadrupole moment of ${}^7\text{Li}$, by considering *ab initio* calculations for the ratio of quadrupole moments for these mirror nuclei, as discussed in Ref. [13], where an estimate $Q_p \approx -6.8$ fm² was obtained for the

unmeasured ${}^7\text{Be}$ quadrupole moment.

We alternatively use the dimensionless ratio to estimate an unmeasured radius from a measured quadrupole moment taking, for example, ${}^8\text{B}$ [Fig. 4(b)] and ${}^{12}\text{B}$ [Fig. 4(l)]. The detailed convergence properties, for calculations with the Daejeon16 interaction, are illustrated in Fig. 9.

For ${}^8\text{B}$, the calculated quadrupole moment [Fig. 9(a)] is poorly converged but increasing, with N_{\max} , in the direction of the experimental value $Q(2^+) = +6.43(14)$ fm² [14]. Similarly, extrapolations (small symbols, dotted lines) are scattered, but generally consistent with the experimental value. The calculated ra-

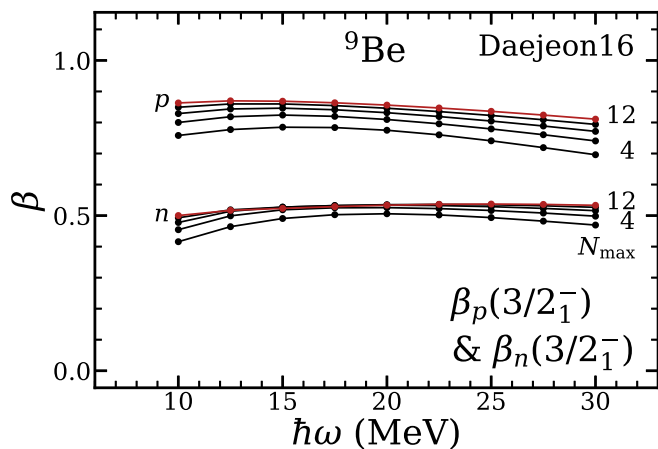


FIG. 10. Calculated deformations for the $3/2^-$ ground state of ${}^9\text{Be}$, as deduced from the ratios of the form Q/r^2 , under the assumption of axially symmetric rotation. Shown are β_p and β_n , for the proton and neutron distributions, respectively (as labeled). Results are obtained with the Daejeon16 interaction. Calculated values are shown as functions of the basis parameter $\hbar\omega$, for successive even values of N_{max} , from $N_{\text{max}} = 4$ to 12 (as labeled).

dius [Fig. 9(c)], while showing indications of shouldering, and exhibiting a crossing point (for curves of successive N_{max}) at $\hbar\omega \gtrsim 10$ MeV, leaves the radius poorly constrained, though apparently > 2.6 fm (extrapolations suggest ≈ 2.7 fm). Rather than taking the ratio Q/r_p^2 considered thus far, we take the reciprocal and square root to obtain $r_p/Q^{1/2}$ [Fig. 9(e)], from which an estimate for the radius may be read off directly by calibration to the measured quadrupole moment (scale at right). Note that the curves are flattened and compressed, especially in the range $10 \text{ MeV} \leq \hbar\omega \leq 20 \text{ MeV}$, allowing us to read off an estimate of $r \approx 2.7$ fm. However, as seen in Fig. 4(b), the prediction for Q/r_p^2 varies by $\approx 10\%$ among the interactions considered. The estimates of r obtained with these different interactions correspondingly vary, by about half as much ($\approx 5\%$).

We may attempt a similar analysis for ${}^{12}\text{B}$, where again the quadrupole moment is measured and the radius unmeasured. Here the experimental quadrupole moment is nearly a factor of 5 smaller than for ${}^8\text{B}$, with $Q(1^+) = +1.32(3) \text{ fm}^2$ [14]. However, the rationale for estimating the radius from the measured quadrupole moment is undermined by the observation that the Daejeon16 interaction appears to be significantly overestimating the quadrupole moment itself [Fig. 9(b)], even based on the unconverged calculations so far. Directly calculating the radius suggests $r_p \approx 2.2\text{--}2.4$ fm [Fig. 9(d)], while normalizing the relatively well-converged ratio Q/r_p^2 and to the experimental Q provides a lower estimate, of $r_p \approx 2.0$ fm [Fig. 9(f)]. Here again, the predicted ratio has a significant interaction dependence, varying by $\approx 1/3$ over the interactions considered [Fig. 4(l)].

V. DEFORMATION

Finally, let us explore what the ratios of the form Q/r^2 indicate for the ground state deformation, via the rotational relation (13). We first illustrate with the ${}^9\text{Be}$ ground state, in Fig. 10, which we take to be the band head of a rotational band with $K = 3/2$ [11, 77]. In addition to the ratio Q/r_p^2 of proton observables (or, for consistency of notation across protons and neutrons, Q_p/r_p^2), which yields β_p (upper curves), we consider the corresponding ratio Q_n/r_n^2 of neutron observables, which yields β_n (lower curves). [The curves for β_p show the same underlying dimensionless ratio as in Fig. 2(j), simply rescaled according to (13).] Note the much smaller calculated deformation for the neutrons, by nearly a factor of 2. Such is to be expected in a cluster molecular orbital interpretation [78–80], in which ${}^9\text{Be}$ is an α - α dimer plus a covalent neutron, when the neutron occupies an equatorial (π) orbital about the molecular symmetry axis, leading to a more spherical shape. This cluster interpretation is supported by densities obtained with NCCI calculations (see Fig. 7 of Ref. [3]).

Turning to the boron isotopes, shown in Fig. 11, the ground state angular momenta for all these isotopes support a quadrupole moment ($J \geq 1$). For each isotope, the deformation is extracted from the quadrupole moment and radius, on the assumption that the ground state is a rotational band head, that is, taking $K = J$ in (13).⁷ We again consider both the ratio of proton observables, for β_p [Fig. 11 (top)], and that of neutron observables, for β_n [Fig. 11 (bottom)]. The calculated ratios Q/r_p^2 themselves vary by almost an order of magnitude across these isotopes: ${}^8\text{B}$ [Fig. 4(b)], ${}^9\text{B}$ [Fig. 4(c)], ${}^{10}\text{B}$ [Fig. 5(b)], ${}^{11}\text{B}$ [Fig. 4(k)], and ${}^{12}\text{B}$ [Fig. 4(l)]. However, after application of the rotational relation (13), the proton deformations are relatively constant, at $\beta_p \approx 0.5$, across the isotopic chain [Fig. 11 (top)]. In contrast, the neutron deformation starts at $\beta_n \approx 0.5$ for ${}^8\text{B}$ [Fig. 11(f)], peaks at $\beta_n \approx 0.8$ for ${}^9\text{B}$ [Fig. 11(g)], then steadily decreases to $\beta_n \approx 0.1\text{--}0.2$ for ${}^{12}\text{B}$ [Fig. 11(j)].

VI. CONCLUSION

Although *ab initio* predictions of nuclear $E2$ observables are hampered by poor convergence in NCCI calculations, correlations among calculated observables can be

⁷ Within a rotational picture, a $J = 3/2$ ground state could alternatively be a member of a $K = 1/2$ band, if the energies are inverted due to Coriolis decoupling, as in ${}^7\text{Be}$ [11, 77]. Furthermore, a $J = 1$ ground state could alternatively be a member of a $K = 0$ band with odd signature [51]. Nonetheless, the calculated low-energy spectra for ${}^9,{}^{11},{}^{12}\text{B}$ are consistent with a simple $K = J$ assignment, as is also expected for these nuclei from SU(3) symmetry arguments [77].

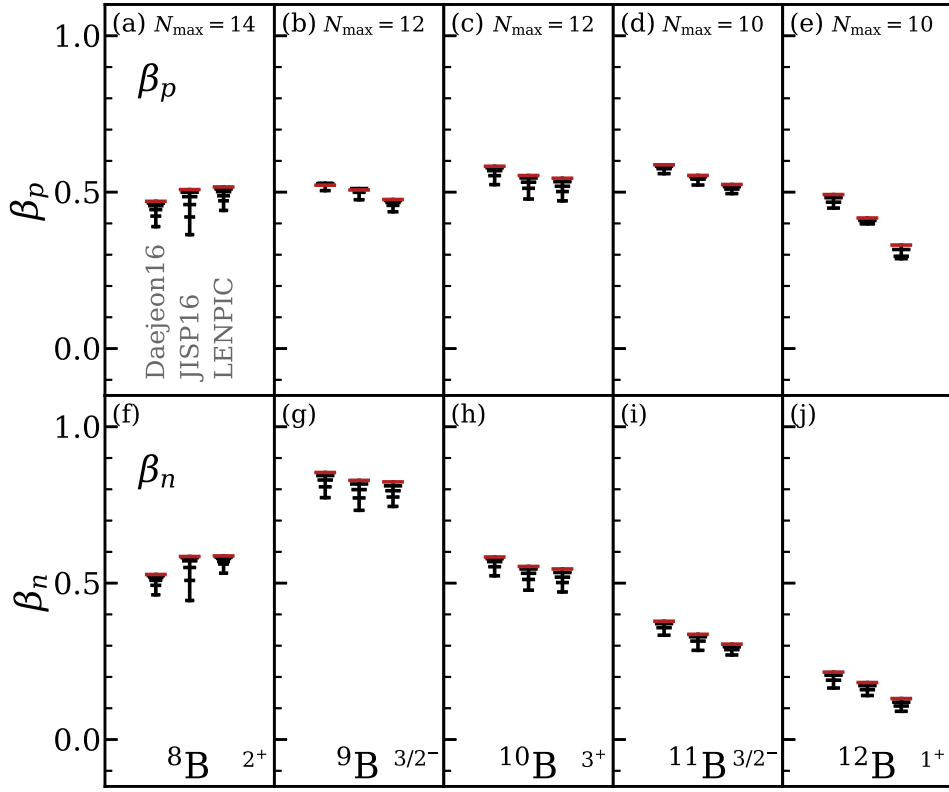


FIG. 11. Calculated deformations for the ground states of the p -shell B isotopes ($N = 3-7$, left to right), as deduced from the ratios of the form Q/r^2 , under the assumption of axially symmetric rotation. Shown are β_p (top) and β_n (bottom), for the proton and neutron distributions, respectively. Results are obtained with the Daejeon16, JISP16, and LENPIC interactions (from left to right, within each panel). Calculated values are shown at fixed $\hbar\omega = 20$ MeV and varying N_{\max} (increasing tick size), from $N_{\max} = 4$ to the maximum value indicated (at top). In each case it is assumed that $K = J$, where the ground state quantum numbers are indicated for reference (at bottom).

exploited to extract meaningful predictions. In particular, systematic truncation errors can cancel in appropriate dimensionless ratios of observables, leading to more robust convergence, as we explore here for dimensionless ratios of the form Q/r^2 , involving quadrupole moment and radius observables.

The nuclear ground state charge radius and/or quadrupole moment are well-measured for many nuclei. If both are known, a robustly converged *ab initio* prediction of the ratio Q/r_p^2 provides a test of the *ab initio* description, including structural features which may be sensitive to the interaction. If only the charge radius is well-measured, a robust *ab initio* prediction of the ratio Q/r_p^2 effectively yields a prediction for the quadrupole moment itself. In practice, however, the quadrupole moment is more often measured, while the radius is still unknown, in which case, conversely, an *ab initio* prediction for Q/r_p^2 yields a prediction for the unmeasured radius, as illustrated here for ${}^8\text{B}$. Similar observations apply to neutron quadrupole moment and radius observables, to the extent that they may be experimentally accessible.

Moreover, robustly calculated ratios of the form Q/r^2 , for both proton and neutron observables, provide insight into the nuclear quadrupole deformation. In an axial ro-

tational description, these ratios measure the quadrupole deformation parameter β . In calculations for the p -shell B isotopes, we find an essentially constant proton deformation, and a smooth evolution in neutron deformation peaking just below mid-shell.

ACKNOWLEDGMENTS

We thank James P. Vary, Ik Jae Shin, and Youngman Kim for sharing illuminating results on ratios of observables, Patrick J. Fasano and Peter Mueller for valuable discussions, and Scott R. Carmichael and Shwetha L. Vittal for comments on the manuscript. This material is based upon work supported by the U.S. Department of Energy, Office of Science, under Awards No. DE-FG02-95ER40934 and No. DE-SC0023495 (SciDAC5/NUCLEI). This research used resources of the National Energy Research Scientific Computing Center (NERSC), a DOE Office of Science User Facility supported by the Office of Science of the U.S. Department of Energy under Contract No. DE-AC02-05CH11231, using NERSC awards NP-ERCAP0020422 and NP-ERCAP0023497.

Appendix A: Relations for exponential convergence

Under the assumption of exponential convergence, of the form (18),

$$X(N_{\max}) = X_{\infty} + a \exp(-cN_{\max}),$$

it is readily verified, *e.g.*, from the standard closed form for a geometric series [81], that the difference between the limiting value X_{∞} and the last calculated value X may be related to the size Δ of the last step taken, in terms of the ratio η of the sizes of successive steps. Namely,

$$X_{\infty} - X = \frac{\eta}{1 - \eta} \Delta. \quad (\text{A1})$$

In the familiar case of Zeno's paradox, where each step that one takes is half the size of the preceding step ($\eta = 1/2$), each step brings one half-way to limiting value (*i.e.*, the "finish line"). Consequently, to reach the limiting value, one must proceed as far again as in the last step taken. From (A1), we indeed recover $X_{\infty} - X = \Delta$. Then, for example, for $\eta = 2/3$, one must proceed twice as far again as in the last step taken; for $\eta = 3/4$, one

must proceed 3 times as far; for $\eta = 4/5$, one must proceed 4 times as far, *etc.*

Given three consecutive calculated values, namely, $X(N_{\max} - 4)$, $X(N_{\max} - 2)$, and $X(N_{\max})$, an exponential fit (18) to these three points is exact. From this same observation (A1), we may extract the value of X_{∞} corresponding to this exact fit analytically (that is, rather than by numerical least-squares fitting) simply by evaluating

$$X_{\infty} = X(N_{\max}) - \frac{\eta(N_{\max})}{\eta(N_{\max}) - 1} \Delta(N_{\max}), \quad (\text{A2})$$

in terms of

$$\Delta(N_{\max}) = X(N_{\max}) - X(N_{\max} - 2) \quad (\text{A3})$$

and

$$\eta(N_{\max}) = \frac{\Delta(N_{\max})}{\Delta(N_{\max} - 2)}, \quad (\text{A4})$$

where here we have reexpressed (17) in terms of Δ . For simplicity of notation in the above expressions, we have not explicitly labeled Δ or η by the observable X to which they correspond (as in Sec. III).

-
- [1] M. Pervin, S. C. Pieper, and R. B. Wiringa, Quantum Monte Carlo calculations of electroweak transition matrix elements in $A = 6, 7$ nuclei, *Phys. Rev. C* **76**, 064319 (2007).
- [2] S. K. Bogner, R. J. Furnstahl, P. Maris, R. J. Perry, A. Schwenk, and J. Vary, Convergence in the no-core shell model with low-momentum two-nucleon interactions, *Nucl. Phys. A* **801**, 21 (2008).
- [3] P. Maris and J. P. Vary, *Ab initio* nuclear structure calculations of p -shell nuclei with JISP16, *Int. J. Mod. Phys. E* **22**, 1330016 (2013).
- [4] J. Carlson, S. Gandolfi, F. Pederiva, S. C. Pieper, R. Schiavilla, K. E. Schmidt, and R. B. Wiringa, Quantum Monte Carlo methods for nuclear physics, *Rev. Mod. Phys.* **87**, 1067 (2015).
- [5] D. Odell, T. Papenbrock, and L. Platter, Infrared extrapolations of quadrupole moments and transitions, *Phys. Rev. C* **93**, 044331 (2016).
- [6] R. Roth and M. Petri, Electromagnetic properties of nuclei from first principles: A case for synergies between experiment and theory, *Philos. Trans. R. Soc. London A* **382**, 2023011902024 (2023).
- [7] B. R. Barrett, P. Navrátil, and J. P. Vary, *Ab initio* no core shell model, *Prog. Part. Nucl. Phys.* **69**, 131 (2013).
- [8] A. Calci and R. Roth, Sensitivities and correlations of nuclear structure observables emerging from chiral interactions, *Phys. Rev. C* **94**, 014322 (2016).
- [9] M. A. Caprio, P. Maris, and J. P. Vary, Emergence of rotational bands in *ab initio* no-core configuration interaction calculations of light nuclei, *Phys. Lett. B* **719**, 179 (2013); P. Maris, M. A. Caprio, and J. P. Vary, Emergence of rotational bands in *ab initio* no-core configuration interaction calculations of the Be isotopes, *Phys. Rev. C* **91**, 014310 (2015); Erratum: Emergence of rotational bands in *ab initio* no-core configuration interaction calculations of the Be isotopes, *Phys. Rev. C* **99**, 029902(E) (2019).
- [10] M. A. Caprio, P. J. Fasano, A. E. McCoy, P. Maris, and J. P. Vary, *Ab initio* rotation in ^{10}Be , *Bulg. J. Phys.* **46**, 445 (2019).
- [11] M. A. Caprio, P. J. Fasano, P. Maris, A. E. McCoy, and J. P. Vary, Probing *ab initio* emergence of nuclear rotation, *Eur. Phys. J. A* **56**, 120 (2020).
- [12] S. L. Henderson, T. Ahn, M. A. Caprio, P. J. Fasano, A. Simon, W. Tan, P. O'Malley, J. Allen, D. W. Bardayan, D. Blankstein, B. Frentz, M. R. Hall, J. J. Kolata, A. E. McCoy, S. Moylan, C. S. Reingold, S. Y. Strauss, and R. O. Torres-Isea, First measurement of the $B(E2; 3/2^- \rightarrow 1/2^-)$ transition strength in ^7Be : Testing *ab initio* predictions for $A = 7$ nuclei, *Phys. Rev. C* **99**, 064320 (2019).
- [13] M. A. Caprio, P. J. Fasano, P. Maris, and A. E. McCoy, Quadrupole moments and proton-neutron structure in p -shell mirror nuclei, *Phys. Rev. C* **104**, 034319 (2021).
- [14] N. J. Stone, Table of nuclear electric quadrupole moments, *At. Data Nucl. Data Tables* **111–112**, 1 (2016).
- [15] M. A. Caprio and P. J. Fasano, *Ab initio* estimation of $E2$ strengths in ^8Li and its neighbors by normalization to the measured quadrupole moment, *Phys. Rev. C* **106**, 034320 (2022).
- [16] H. Li, D. Fang, H. J. Ong, A. M. Shirokov, J. P. Vary, P. Yin, and X. Zhao, Quadrupole dynamics of carbon isotopes and ^{10}Be (2024), arXiv:2401.05776 [nucl-th].
- [17] I. Angeli and K. P. Marinova, Table of experimental nu-

- clear ground state charge radii: An update, *At. Data Nucl. Data Tables* **99**, 69 (2013).
- [18] J. H. Kelley, J. E. Purcell, and C. G. Sheu, Energy levels of light nuclei $A = 12$, *Nucl. Phys. A* **968**, 71 (2017).
- [19] D. R. Tilley, C. M. Cheves, J. L. Godwin, G. M. Hale, H. M. Hofmann, J. H. Kelley, C. G. Sheu, and H. R. Weller, Energy levels of light nuclei $A = 5, 6, 7$, *Nucl. Phys. A* **708**, 3 (2002).
- [20] D. R. Tilley, J. H. Kelley, J. L. Godwin, D. J. Millener, J. E. Purcell, C. G. Sheu, and H. R. Weller, Energy levels of light nuclei $A = 8, 9, 10$, *Nucl. Phys. A* **745**, 155 (2004).
- [21] J. H. Kelley, E. Kwan, J. E. Purcell, C. G. Sheu, and H. R. Weller, Energy levels of light nuclei $A = 11$, *Nucl. Phys. A* **880**, 88 (2012).
- [22] F. Ajzenberg-Selove, Energy levels of light nuclei $A = 13-15$, *Nucl. Phys. A* **523**, 1 (1991).
- [23] R. Neugart and G. Neyens, Nuclear moments, in *The Euroschool Lectures on Physics with Exotic Beams, Vol. II*, Lecture Notes in Physics, Vol. 700, edited by J. Al-Khalili and E. Roeckl (Springer-Verlag, Berlin, 2006) p. 135.
- [24] X. F. Yang, S. J. Wang, S. G. Wilkins, and R. F. Garcia Ruiz, Laser spectroscopy for the study of exotic nuclei, *Prog. Part. Nucl. Phys.* **129**, 104005 (2023).
- [25] A. Bohr, The coupling of nuclear surface oscillations to the motion of individual nucleons, *Mat. Fys. Medd. Dan. Vid. Selsk.* **26** (1952).
- [26] D. J. Rowe, Microscopic theory of the nuclear collective model, *Rep. Prog. Phys.* **48**, 1419 (1985).
- [27] A. Bernstein, V. Brown, and V. Madsen, Neutron and proton matrix elements for low-lying 2^+ transitions and the probe dependence of the nuclear deformation parameter, *Comments Nucl. Part. Phys.* **11**, 203 (1983).
- [28] B. Jonson, Light dripline nuclei, *Phys. Rep.* **389**, 1 (2004).
- [29] I. Tanihata, H. Savajols, and R. Kanungo, Recent experimental progress in nuclear halo structure studies, *Prog. Part. Nucl. Phys.* **68**, 215 (2013).
- [30] T. Furuno, T. Kawabata, S. Adachi, Y. Ayyad, Y. Kanada-En'yo, Y. Fujikawa, K. Inaba, M. Murata, H. J. Ong, M. Sferrazza, Y. Takahashi, T. Takeda, I. Tanihata, D. T. Tran, and M. Tsumura, Neutron quadrupole transition strength in ^{10}C deduced from the $^{10}\text{C}(\alpha, \alpha')$ measurement with the MAIKO active target, *Phys. Rev. C* **100**, 054322 (2019).
- [31] V. V. Flambaum, V. A. Dzuba, and C. Harabati, Effect of nuclear quadrupole moments on parity nonconservation in atoms, *Phys. Rev. A* **96**, 012516 (2017).
- [32] G. Arrowsmith-Kron, M. Athanasakis-Kaklamanakis, M. Au, J. Ballof, R. Berger, A. Borschevsky, A. A. Breier, F. Buchinger, D. Budker, L. Caldwell, C. Charles, N. Dattani, R. P. de Groote, D. DeMille, T. Dickel, J. Dobaczewski, C. E. Düllmann, E. Eliav, J. Engel, M. Fan, V. Flambaum, K. T. Flanagan, A. N. Gaiser, R. F. Garcia Ruiz, G. Gaul, T. F. Giesen, J. S. M. Ginges, A. Gottberg, G. Gwinner, R. Heinke, S. Hoekstra, J. D. Holt, N. R. Hutzler, A. Jayich, J. Kartheim, K. G. Leach, K. W. Madison, S. Malbrunot-Ettenauer, T. Miyagi, I. D. Moore, S. Moroch, P. Navratil, W. Nazarewicz, G. Neyens, E. B. Norrgard, N. Nusgart, L. F. Pařteka, A. N. Petrov, W. R. Plaß, R. A. Ready, M. P. Reiter, M. Reponen, S. Rothe, M. S. Safronova, C. Scheiden-erger, A. Shindler, J. T. Singh, L. V. Skripnikov, A. V. Titov, S.-M. Udrescu, S. G. Wilkins, and X. Yang, Opportunities for fundamental physics research with radioactive molecules, *Rep. Prog. Phys.* **87**, 084301 (2024).
- [33] M. A. Caprio *et al.*, Robust *ab initio* predictions for dimensionless ratios of $E2$ and radius observables. II. Estimation of $E2$ strengths by calibration to the charge radius (in preparation).
- [34] K. Heyde and J. L. Wood, Shape coexistence in atomic nuclei, *Rev. Mod. Phys.* **83**, 1467 (2011).
- [35] A. E. McCoy, M. A. Caprio, P. Maris, and P. J. Fasano, Intruder band mixing in an *ab initio* description of ^{12}Be , *Phys. Lett. B* **856**, 138870 (2024).
- [36] M. A. Caprio, P. J. Fasano, and P. Maris, Robust *ab initio* prediction of nuclear electric quadrupole observables by scaling to the charge radius, *Phys. Rev. C* **105**, L061302 (2022).
- [37] J. Suhonen, *From Nucleons to Nucleus* (Springer-Verlag, Berlin, 2007).
- [38] A. R. Edmonds, *Angular Momentum in Quantum Mechanics*, 2nd ed., Investigations in Physics No. 4 (Princeton University Press, Princeton, New Jersey, 1960).
- [39] D. A. Varshalovich, A. N. Moskalev, and V. K. Khersonskii, *Quantum Theory of Angular Momentum* (World Scientific, Singapore, 1988).
- [40] M. A. Caprio, A. E. McCoy, and P. J. Fasano, Intrinsic operators for the translationally-invariant many-body problem, *J. Phys. G* **47**, 122001 (2020).
- [41] J. L. Friar and J. W. Negele, Theoretical and experimental determination of nuclear charge distributions, in *Advances in Nuclear Physics*, Vol. 8, edited by M. Baranger and E. Vogt (Plenum, New York, 1975) p. 219.
- [42] J. L. Friar, Pion-exchange contributions to the nuclear charge, current, and Hamiltonian operators, *Ann. Phys. (N.Y.)* **104**, 380 (1977).
- [43] J. L. Friar, Retardation, quasipotential equations, and relativistic corrections to the deuteron charge operator, *Phys. Rev. C* **22**, 796 (1980).
- [44] J. L. Friar, J. Martorell, and D. W. L. Sprung, Nuclear sizes and the isotope shift, *Phys. Rev. A* **56**, 4579 (1997).
- [45] Z.-T. Lu, P. Mueller, G. W. F. Drake, W. Nörtershäuser, S. C. Pieper, and Z.-C. Yan, Laser probing of neutron-rich nuclei in light atoms, *Rev. Mod. Phys.* **85**, 1383 (2013).
- [46] R. L. Workman *et al.* (Particle Data Group), Review of particle physics, *Prog. Exp. Theor. Phys.* **2022**, 083C01 (2022).
- [47] S. Pastore, L. Girlanda, R. Schiavilla, and M. Viviani, Two-nucleon electromagnetic charge operator in chiral effective field theory (χEFT) up to one loop, *Phys. Rev. C* **84**, 024001 (2011).
- [48] S. Kölling, E. Epelbaum, H. Krebs, and U.-G. Meißner, Two-nucleon electromagnetic current in chiral effective field theory: One-pion exchange and short-range contributions, *Phys. Rev. C* **84**, 054008 (2011).
- [49] H. Krebs, Nuclear currents in chiral effective field theory, *Eur. Phys. J. A* **56**, 234 (2020).
- [50] A. Ong, J. C. Berengut, and V. V. Flambaum, Effect of spin-orbit nuclear charge density corrections due to the anomalous magnetic moment on halonuclei, *Phys. Rev. C* **82**, 014320 (2010).
- [51] D. J. Rowe, *Nuclear Collective Motion: Models and Theory* (World Scientific, Singapore, 2010).
- [52] J. M. Eisenberg and W. Greiner, *Nuclear Models: Col-*

- lective and Single-Particle Phenomena*, 3rd ed., Nuclear Theory, Vol. 1 (North-Holland, Amsterdam, 1987).
- [53] J. Meyer-ter-Vehn, Collective model description of transitional odd- A nuclei: (I). The triaxial-rotor-plus-particle model, Nucl. Phys. A **249**, 111 (1975).
- [54] O. Castaños, J. P. Draayer, and Y. Leschber, Shape variables and the shell model, Z. Phys. A **329**, 33 (1988).
- [55] S. Raman, C. W. Nestor, Jr., and P. Tikkanen, Transition probability from the ground to the first-excited 2^+ state of even-even nuclides, At. Data Nucl. Data Tables **78**, 1 (2001).
- [56] B. Pritychenko, M. Birch, B. Singh, and M. Horoi, Tables of $E2$ transition probabilities from the first 2^+ states in even-even nuclei, At. Data Nucl. Data Tables **107**, 1 (2016).
- [57] S. Pastore, S. C. Pieper, R. Schiavilla, and R. B. Wiringa, Quantum Monte Carlo calculations of electromagnetic moments and transitions in $A \leq 9$ nuclei with meson-exchange currents derived from chiral effective field theory, Phys. Rev. C **87**, 035503 (2013).
- [58] P. Maris, M. Sosonkina, J. P. Vary, E. Ng, and C. Yang, Scaling of ab-initio nuclear physics calculations on multicore computer architectures, Procedia Comput. Sci. **1**, 97 (2010); M. Shao, H. M. Aktulga, C. Yang, E. G. Ng, P. Maris, and J. P. Vary, Accelerating nuclear configuration interaction calculations through a preconditioned block iterative eigensolver, Comput. Phys. Commun. **222**, 1 (2018).
- [59] A. M. Shirokov, I. J. Shin, Y. Kim, M. Sosonkina, P. Maris, and J. P. Vary, N³LO NN interaction adjusted to light nuclei in *ab exitu* approach, Phys. Lett. B **761**, 87 (2016).
- [60] A. M. Shirokov, J. P. Vary, A. I. Mazur, and T. A. Weber, Realistic nuclear Hamiltonian: *Ab exitu* approach, Phys. Lett. B **644**, 33 (2007).
- [61] E. Epelbaum, H. Krebs, and U.-G. Meißner, Precision nucleon-nucleon potential at fifth order in the chiral expansion, Phys. Rev. Lett. **115**, 122301 (2015).
- [62] E. Epelbaum, H. Krebs, and U.-G. Meißner, Improved chiral nucleon-nucleon potential up to next-to-next-to-next-to-leading order, Eur. Phys. J. A **51**, 53 (2015).
- [63] D. R. Entem and R. Machleidt, Accurate charge-dependent nucleon-nucleon potential at fourth order of chiral perturbation theory, Phys. Rev. C **68**, 041001(R) (2003).
- [64] S. K. Bogner, R. J. Furnstahl, and R. J. Perry, Similarity renormalization group for nucleon-nucleon interactions, Phys. Rev. C **75**, 061001(R) (2007).
- [65] M. A. Caprio, P. Maris, and J. P. Vary, Halo nuclei ${}^6\text{He}$ and ${}^8\text{He}$ with the Coulomb-Sturmian basis, Phys. Rev. C **90**, 034305 (2014).
- [66] P. J. Fasano, Ch. Constantinou, M. A. Caprio, P. Maris, and J. P. Vary, Natural orbitals for the *ab initio* no-core configuration interaction approach, Phys. Rev. C **105**, 054301 (2022).
- [67] P. Maris, J. P. Vary, and A. M. Shirokov, *Ab initio* no-core full configuration calculations of light nuclei, Phys. Rev. C **79**, 014308 (2009).
- [68] See Supplemental Material at <http://xxxxxxx> for comprehensive plots and tabulations of the calculated observables, as functions of N_{max} and $\hbar\omega$.
- [69] R. B. Wiringa, V. G. J. Stoks, and R. Schiavilla, Accurate nucleon-nucleon potential with charge-independence breaking, Phys. Rev. C **51**, 38 (1995).
- [70] S. C. Pieper, The Illinois extension to the Fujita-Miyazawa three-nucleon force, in *New Facet of Three Nucleon Force — 50 Years of Fujita Miyazawa Three Nucleon Force (FM50): Proceedings of the International Symposium on New Facet of Three Nucleon Force*, AIP Conf. Proc. No. 1011, edited by H. Sakai, K. Sekiguchi, and B. F. Gibson (AIP, New York, 2008) pp. 143–152.
- [71] S. C. Pieper and J. Carlson, as cited in Ref. [4].
- [72] M. Seya, M. Kohno, and S. Nagata, Nuclear binding mechanism and structure of neutron-rich Be and B isotopes by molecular-orbital model, Prog. Theor. Phys. **65**, 204 (1981).
- [73] M. Freer, The clustered nucleus—cluster structures in stable and unstable nuclei, Rep. Prog. Phys. **70**, 2149 (2007).
- [74] K. R. Henninger, T. Neff, and H. Feldmeier, ${}^8\text{B}$ structure in fermionic molecular dynamics, J. Phys. Conf. Ser. **599**, 012038 (2015).
- [75] V. F. Weisskopf, Radiative transition probabilities in nuclei, Phys. Rev. **83**, 1073 (1951).
- [76] C. Cockrell, J. P. Vary, and P. Maris, Lithium isotopes within the *ab initio* no-core full configuration approach, Phys. Rev. C **86**, 034325 (2012).
- [77] D. J. Millener, Hypernuclear gamma-ray spectroscopy and the structure of p -shell nuclei and hypernuclei, in *Topics in Strangeness Nuclear Physics*, Lecture Notes in Physics, Vol. 724, edited by P. Bydžovský, J. Mareš, and A. Gal (Springer, Berlin, 2007) p. 31.
- [78] S. Okabe, Y. Abe, and H. Tanaka, The structure of ${}^9\text{Be}$ nucleus by a molecular model. I, Prog. Theor. Phys. **57**, 866 (1979).
- [79] W. von Oertzen, Two-center molecular states in ${}^9\text{B}$, ${}^9\text{Be}$, ${}^{10}\text{Be}$, and ${}^{10}\text{B}$, Z. Phys. A **354**, 37 (1996).
- [80] Y. Kanada-En'yo, H. Horiuchi, and A. Doté, Structure of excited states of ${}^{10}\text{Be}$ studied with antisymmetrized molecular dynamics, Phys. Rev. C **60**, 064304 (1999).
- [81] F. W. J. Olver, D. W. Lozier, R. F. Boisvert, and C. W. Clark, eds., *NIST Handbook of Mathematical Functions* (Cambridge University Press, Cambridge, 2010).